

9. Joining

A. Forming Limits of Weld Metal in Aluminum Alloys and Advanced High-Strength Steels

Principal Investigators: Richard W. Davies, Elizabeth V. Stephens and Glenn J. Grant
Pacific Northwest National Laboratory
P.O. Box 999, Richland, WA 99352-0999
(509) 375-6474; e-mail: rich.davies@pnl.gov

Industry Consultants/Participants: General Motors, Chrysler, Ford, U.S. Steel, Olympic Controls, Alcoa

Technology Area Development Manager: William Joost
(202)257-6020; e-mail: william.joost@ee.doe.gov

Field Technical Manager: Mark T. Smith
(509) 375-4478; e-mail: mark.smith@pnl.gov

Contractor: Pacific Northwest National Laboratory
Contract No.: DE-AC05-76RL01830

Objective

- Develop, validate and disseminate a combined experimental and numerical method to describe (statistically) and quantify (systematically) the forming limits of welded aluminum alloys and high-strength steels.
- Provide industry users with a low-cost and reliable experimental and analytical tool for use in the design, processing and application of welded aluminum and high strength steels for tailor-welded blanks and hydroforming preforms.

Approach

- Develop a standard tool for weld process development that will systematically quantify failure probabilities during forming.
- Provide accurate, standardized methods of experimentally characterizing weld metal formability using unique but simple test methods available on the shop floor.
- Provide predictive models for more accurate forming simulations of tailor-welded blanks (TWBs) and hydroforming operations. Predict parts-per-thousand failure rates during production from finite element analysis.
- Characterize static properties and forming behavior of several weld populations and correlate with statistical-based tool.
- Demonstrate application of the weld metal formability tools for biaxial forming of welded aluminum and high strength steel sheet.

Milestone, Metrics and Accomplishments

- Milestone 1 - Established an industrially relevant procedure to determine the forming limit diagram (FLD) of welded DP600 steel alloys. (Completed) The fully-integrated analysis and testing procedure was demonstrated for an industry-supplied DP600 steel welded sheet population. The procedure and results were presented to the industry consulting group.
- Developed a more general procedure that can be applied to welded thin sheets.
- Completed the combined forming limit prediction for DP600, AA5182-6111 and AA5182 welded alloys.
- Quantified the combined FLD using the statistical approach for each welded alloy population.
- Conducted program review meeting in October 2009 to Industrial Team Advisory Committee.

Future Direction

- The technical work on this project was completed in FY2009.
- A peer review publication to commercialize the technology is being prepared.

Introduction

This work is a collaborative effort between DOE, Pacific Northwest National Laboratory (PNNL), U.S. Automotive Materials Partnership (USAMP) team of the U.S. Council for Automotive Research, U.S. Steel, Olympic Controls and Alcoa. This project will develop, validate and disseminate combined experimental and numerical methods that systematically quantify the forming limits of weld materials in aluminum alloys and high-strength steels through a combination of experimental and deformation modeling analysis. This work will enable high-volume, robust deployment of tailor-welded blanks (TWB) and seam- and tailor-welded tubes in emerging materials. [Figure 1](#) is a schematic of the possible vehicle manufacturing applications and relevant current and future materials for the technology.

The deformation of weld materials and their limits of formability are important aspects to both TWB and hydroforming technologies. The conventional low-carbon steels used in automotive applications are easily fusion-welded using conventional technologies and suffer no appreciable strength degradation near the weld. Aluminum alloys are more difficult to weld than low-carbon steels due to high conductivity and reflectivity as well as low-molten viscosity. Aluminum also has a high propensity for porosity to form during fusion welding as well as hot cracking and heat-affected zone (HAZ)-related issues in heat-treatable aluminum alloys. Many of the high-strength steel alloys that are finding increased application in the automotive industry suffer from degradation of strength in the HAZ. Further, nearly all fusion welds suffer from irregular geometries and elevated levels of surface roughness compared to the parent materials, which also influence formability and component performance.

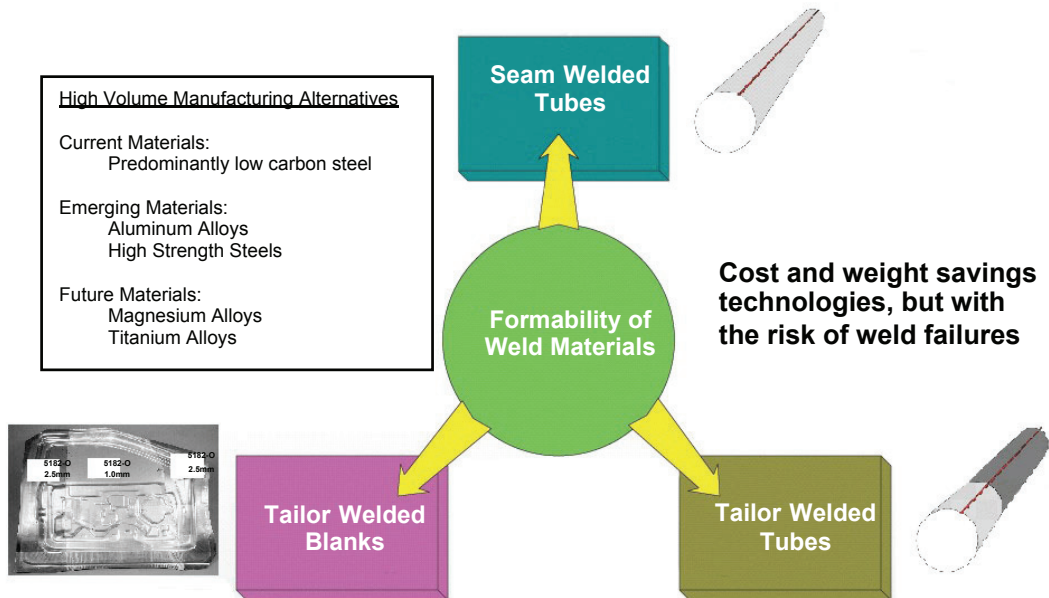


Figure 1. A schematic of the formability of weld materials project and applications where welds are formed during vehicle manufacturing.

This project has focused on developing a generalized numerical method to predict forming limits in weld materials and verifying deformation and forming limit predictions. The approach relies on developing standardized test methods for weld material populations to establish a statistical description of material imperfection and mechanical properties in their weld region and developing statistically based forming limit diagrams (FLD) or continuum damage models that predict material failure in the weld region.

The project includes numerical model development, validation and supporting experiments. A number of candidate weld methods have been examined in combination with selected aluminum alloys and high-strength steels. The principal materials of interest have been aluminum alloys AA5182, AA6061, and DP600 steel. The selection of sheet materials and welding methods were coordinated with the participating original equipment manufacturers (OEMs) and are representative of high-volume commercially viable materials and processing technologies. The deliverables include a standard procedure for weld material evaluation coupled with a numerical approach for establishing weld region forming limits. The results will also allow the evaluation and development of candidate weld processes and the interaction between materials and weld parameters. The overall objective is to develop test methods and experimental results to enable the widespread deployment of weight- optimized TWB and tube hydroforming and to avoid weld failures during production. Figure 2 is a schematic of the typical manufacturing process development for tailor welded products.

During fiscal year 2008 and into 2009, much emphasis was spent on developing an industrially relevant procedure to determine the FLD of welded aluminum and high-strength steel alloys. A procedure was first applied to DP600 welded alloys and then generally modified, so the procedure may be applied to aluminum-welded alloys or any thin sheet-welded alloy to determine the forming limit. The following describes results to date and the development of the industrially relevant procedure.

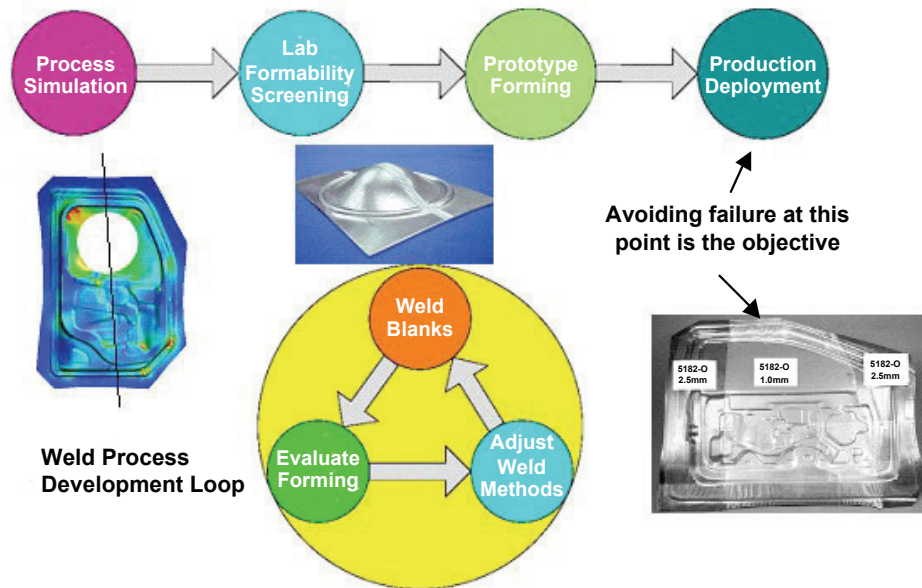


Figure 2. A schematic of the typical manufacturing process development.

M-K Method to Predict Formability

The prediction of TWB formability in this work relies fundamentally upon the Marciniak-Kuczynski (M-K) method coupled to an experimentally-derived measure of weld material imperfection. The M-K method tracks development of plastic strains in the monolithic sheet and weld materials under applied external loading. The M-K method is predicated on the assumption that real materials possess imperfections (or geometric inhomogeneities), and that the strain evolution and eventual localization at the imperfection is the source of failure during metal forming.

In the current work, imperfection levels for a given tailor welded blank population are determined by performing approximately thirty tensile tests in each of the directions longitudinal and transverse to the weld within the TWB. The level of imperfection (f) that must exist in the specimens in order to describe the formability for each of the thirty specimens is determined using M-K methods. Give the localization strain from each test, and the variations in the localization strain, one can establish a statistically-based level of imperfection for each weld population in both the longitudinal and transverse direction.

The Weibull probability distribution has proven to be the most suitable to describe the specimen imperfections, and the predicted FLD for the TWBs is generated using this function. Using this standard function permits an active selection of the level of risk that the practitioner assumes during manufacturing to develop safe forming limit diagrams for a given weld population.

General Procedure in Determining the FLD of Welded Alloys

Currently, there is no industrial standard that describes the formability of TWBs that include the effects of the weld region. The primary goal of this project is to develop a procedure for industry to use by characterizing the variability of these materials to reduce the risk assumed while deploying this weight-saving technology to enable greater commercialization. This project has generated a procedure to describe the forming limit operating envelope of TWB materials. The general procedure was first applied to DP600 welded alloys. Figure 3 depicts the DP600 TWB FLD generated from the 10-step process described below:

1. Establish the thin (or the weaker) sheet FLD and draw a three-quadrant FLD where longitudinal strain is the ordinate (y-axis) and the transverse strain is the abscissa (x-axis) for this material
2. Conduct approximately 30 longitudinal tensile tests and measure the “safe” level of strain in the thin sheet adjacent to the weld for each specimen
3. Calculate the statistical distribution for the level of imperfection for the longitudinal specimens
4. Conduct approximately 30 transverse tensile tests and measure the “safe” level of strain in the thin sheet adjacent to the weld for each specimen and verify that no weld related failures occurred Note: In previously reported work, experimental results showed that in the transverse weld condition, there was no fracture in the weld or in the heat affected zone of the DP600 welded specimens. Localization occurred in the thin sheet, and fracture was determined by the properties of the 1 mm parent sheet material. Therefore, the 1 mm sheet FLD dictates TWB failure in transverse loading conditions.
5. Assume the acceptable failure rate for a given metal forming application (recommendation is 1 part per 1000)
6. Calculate the imperfection level for the longitudinal population that corresponds to the acceptable failure rate
7. Calculate the “safe” level of strain along the longitudinal tensile direction that corresponds to the acceptable failure rate (Locate Point 1 on diagram)
8. Calculate the strain path direction developing in the thin sheet when the weld is being loaded in plane strain longitudinal to the weld and place a point on the FLD that corresponds to the “safe” longitudinal plane strain and the transverse strain in the thin sheet (Locate Point 3 on the diagram)
9. Connect Points 1 and 3 via a line.
10. Draw a horizontal line from Point 3 horizontal to intersect the thin sheet FLD to the right of Point 3.

In Figure 3, the safe FLD for this TWB population is defined as the condition where no more than 1 part per 1000 parts formed will fail under biaxial stretching. In practice, the working strain during forming should be limited such that it remains under the 1 part per 1000 forming limit and the thin sheet FLD in the transverse direction.

In order to validate this approach, a set of biaxial forming experiments were conducted with the identical TWB population. Figure 4 illustrates the LDH (limiting dome height) results of biaxial experiments in near biaxial stretching, and the shows the loading applied and lubrication used during these experiments. This set of tests compares the failure strain when sheet is loaded biaxially, and permits comparison of predicted and actual failure strains. Figure 5 compares this biaxial data to the predicted FLD for the given weld population. The biaxial data is on or near the 50% failure rate line, which would be expected given a small number of samples.

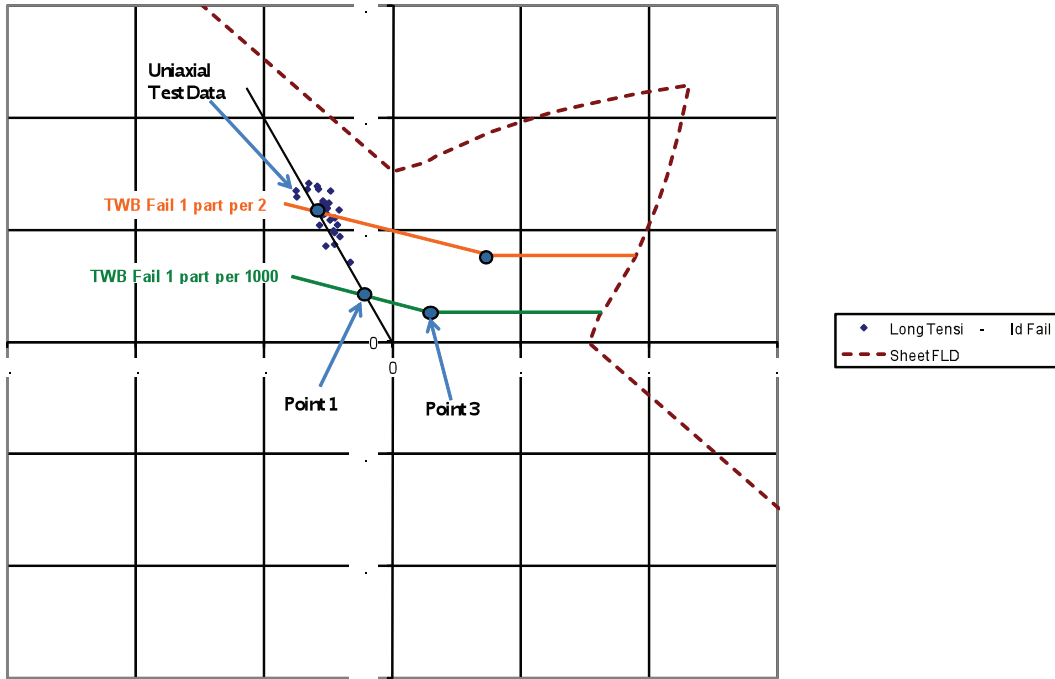


Figure 3. DP600 TWB FLD developed utilizing the industrially relevant procedure.

Photos representative of the LW DP600 specimens after LDH testing. Fracture in the thin sheet observed in all specimens. Table below illustrates the loads and heights observed.



Specimen ID	Specimen Thickness	Lubricant	Clamp Test Load (lb)	Punch Test		Height At Max Load (in.)
				Rate (in./min)	Max Load Detected (lb)	
DP-DP-3	1.5 mm to 1 mm	Teflon	38,000	0.05	20,824	1.05
DP-DP-4	1.5 mm to 1 mm	Teflon	38,000	0.05	20,915	1.06
DP-DP-5	1.5 mm to 1 mm	Teflon	38,000	0.05	19,736	1.03
DP-DP-6	1.5 mm to 1 mm	Teflon	38,000	0.05	19,453	1.01
DP-DP-7	1.5 mm to 1 mm	Teflon	38,000	0.05	18,920	0.98

Figure 4. Illustration of the LDH (limiting dome height) results of biaxial experiments in near biaxial stretching and the applied loading lubrication during these experiments.

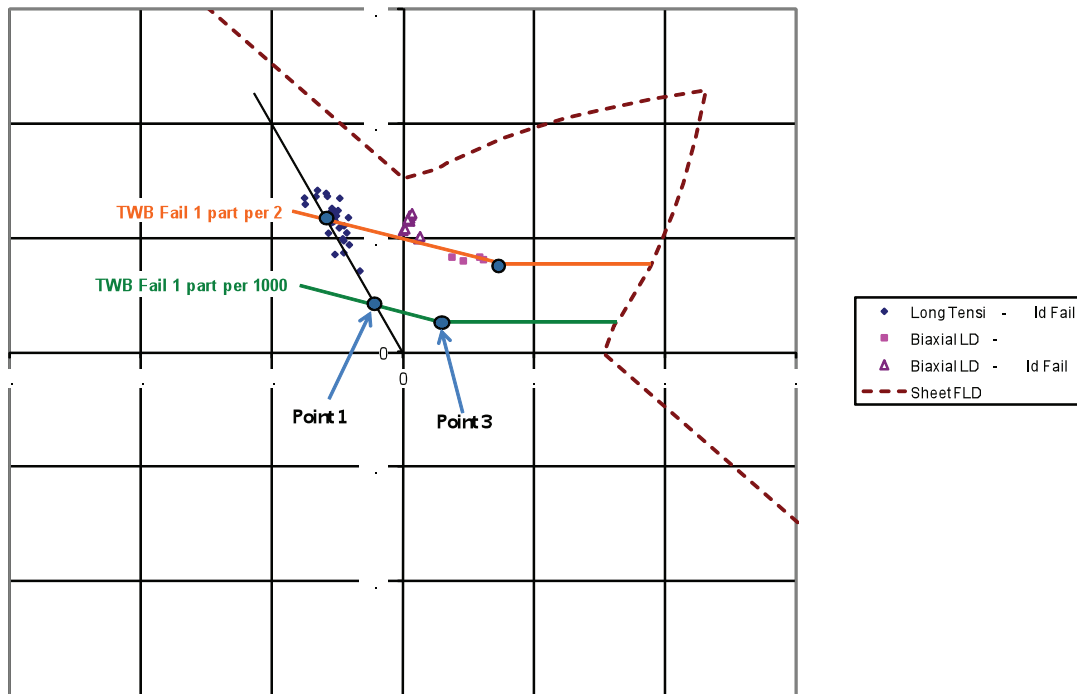


Figure 5. DP600 TWB FLD developed utilizing the industrially relevant procedure compared to a set of biaxial stretching result of the same weld population.

The final activity on this project is producing a peer reviewed publication to enable greater commercialization by reducing the risk assumed while developing and deploying this weight-saving and material-saving technology.

Conclusions

From this investigation, the following conclusions were derived:

- Forming of welds has the potential to simultaneously reduce the cost AND weight of lightweight automotive structures.
- Emerging materials (aluminum and HSS) are generally more challenging to join and form.
- This project has developed a standard approach for describing the forming limits that include the effects of the weld region, which predicts forming failure rates at quantitative levels of deformation.

Presentations/Publications/Patents

- “Forming Limits of Weld Material in Aluminum Alloys and High-Strength Steels.” 2009. Presented to Industrial Team Advisory Committee, Southfield, MI. October 29.

B. Dynamic Characterization of Spot Welds in Advanced High-Strength Steels

Principal Investigator: Zhili Feng
Oak Ridge National Laboratory
1 Bethel Valley Road; Oak Ridge, TN 37831
(865) 576-3797; e-mail: fengz@ornl.gov

Co-Principal Investigator: Srdjan Simunovic
Oak Ridge National Laboratory
1 Bethel Valley Road; Oak Ridge, TN 37831
(865) 241-3863; e-mail: simunovics@ornl.gov

Technology Area Development Manager: Dr. Carol Schutte
(202) 287-5371; e-mail: carol.schutte@ee.doe.gov

Field Technical Monitor: C. David Warren
(865) 574-9693; e-mail: warrencd@ornl.gov

Contractor: Oak Ridge National Laboratory
Contract No.: DE-AC05-00OR22725

Objective

- Develop a new, robust Spot Weld Element (SWE) that can accurately model the deformation and fracture modes of spot welds as a function of impact loading, welding and steel chemistry while maintaining computational efficiency and ease-to-use.
- Develop the implementation procedure to incorporate the SWE in advanced crashworthiness computer aided engineering (CAE) codes used by the automotive crash modelers.
- Generate a companion experimental database on the impact behavior of advanced high-strength steel (AHSS) spot welds under various loading conditions and deformation rates to support and validate the modeling approach.

Approach

- Development of a new spot weld element and associated constitutive models.
- Modeling and characterization of weld microstructure and property.
- Integration of SWE model and weld process and microstructure model.
- Deformation and failure behavior testing under different dynamic loading conditions.

Accomplishments

Successfully completed the Phase I Concept Feasibility development of the SWE modeling framework and demonstrated the effectiveness of such modeling approach in impact simulation of spot welds. Specifically,

- Developed the initial version of SWE
 1. Capable of handling weld geometry and weld property gradient;
 2. Capable of predicting different fracture modes and fracture load limit experimentally observed in impact tests.
- Developed the initial version of integrated electrical-thermal-mechanical-metallurgical resistance spot weld model
 1. Capable of predicting weld geometry, microstructure and microhardness distributions;
 2. Friendly user input interface for welding parameters, sheet thickness and steel chemistry.
- Collected baseline spot weld impact test data on dual phase 780 MPa (DP780) and draw-quality semi-killed (DQSK) steels
 1. Characterization of effects of impact speeds and loading modes;
 2. Web-based database for user-friendly interactive data analysis and retrieval.
- Completed the comprehensive Phase I project report to Department of Energy (DOE) and Auto-Steel Partnership (A/SP).

Future Direction

- Further expand, and validate the SWE model to cover wide range of AHSS grades and spot weld configurations to demonstrate the applicability of SWE for current generation of AHSS.
- Extend to weldbond for AHSS.
- Extend to other materials and joining processes
 1. Joining of steels to other materials (such as Al alloys, Mg alloys, polymer composites) for multi-material body structure;
 2. Friction bit joining, friction stir joining, and laser welding.
- Failure criteria evaluation and development
 1. Incorporate the effect of heat affected zone (HAZ) softening in ultra high-strength steels and Al alloys;
 2. Develop and evaluate failure criteria including the adhesive bonding.
- Further refine SWE formulation for robustness.

Introduction

A primary driver for increased use of advanced high-strength steels (AHSS) and other high strength materials in auto body structures is the improvement in crash performance while reducing the weight. Resistance spot welding (RSW) is by far the most common joining process used in automotive manufacturing. Typically, there are four to five thousand spot welds in a vehicle. Because the separation of spot welds can affect the crash response of a welded structural component, the dynamic behavior of the spot welds under impact loading of vehicle crash has been one of the critically important considerations in vehicle design and manufacturing.

RSW of AHSS presents unique technical challenges for automotive structure applications. Due to their high carbon and alloying element contents, and tailored microstructure, AHSS are considerably more sensitive to the thermal cycle of welding than the conventional steels used in auto body structures. Therefore, RSW of AHSS can exhibit very different structural performance characteristics than the ones made of conventional steels. For example, AHSS RSW generally has higher load-bearing capacity, but can fail under different failure modes (button pullout, interfacial, or mixed). The structural performance of AHSS RSW is highly dependent on the grades and types of AHSS. Furthermore, impact experiments on joints and structural components (top-hat and double-hat sections) have shown that RSW have different responses under static and dynamic loads.

In recent years, CAE based simulation of dynamic (impact) behavior of auto body structures during crash has become an indispensable tool that enables rapid and cost-effective design and engineering of crashworthy auto body structures. However, recent impact crash tests revealed that the prediction of spot-weld failure in crashworthiness CAE simulation of auto body structures made of AHSS is generally unsatisfactory. A gap analysis conducted by A/SP concluded that the industry lacks the fundamental understanding and predictive capability for the spot-weld behavior of AHSS and other light-weight materials (such as Al alloys and Mg alloys) during impact loading of vehicles. These gaps hinder rapid and optimum insertion of AHSS and other lightweight materials in auto body structures. The weld failures, detected in later stages of new model car development cycles, have frequently resulted in design compromises that can adversely affect the weight savings available by using AHSS. Furthermore, lightweighting opportunities from optimized use of AHSS and other lightweight materials will not be possible without improved understanding of the phenomena and the development of respective models and CAE tools for crashworthiness analysis.

This program is aimed at developing a new spot weld modeling methodology, supported by experimental data that can be implemented in crash simulation FEA codes used by the automotive crash modelers. The essential feature of this new model includes, through multi-physics simulation of the spot welding process and the resulting microstructural evolution of materials, a novel spot weld element (SWE) approach capable of handling various deformation and fracture modes, the effects of microstructural and strength variations in spot welds of AHSS and other lightweight materials, and the deformation rates and loading modes encountered in vehicle crash.

A three-prong approach has been adopted in the development of the new spot weld modeling approach:

- A integrated electrical-thermal-mechanical-metallurgical resistance spot weld process model to generate the weld geometry, microstructure and residual stress results needed by SWE,
- A new spot weld element (SWE) and associated constitutive models for its robustness in crashworthiness CAE simulation, and with the complexity to incorporate weld geometry and microstructure effects, and
- A companion weld characterization and impact test database for development and validation of the new spot weld modeling approach.

In recognizing the complexity and the scope of efforts required to develop and mature this new modeling methodology for the wide variety of AHSS currently used in auto-body structures, as well as the use of AHSS and other lightweight materials in future multi-material vehicles, this project was divided into two phases. Phase I was an initial concept feasibility effort to develop and demonstrate the feasibility and potential of the SWE modeling approach for an initial set of steels, weld configurations, and impact testing conditions. Phase II is a comprehensive Technical Feasibility R&D which will cover a wide range of materials, thickness ranges, weld configurations and microstructures, to refine, improve, mature, validate and demonstrate the SWE methodology for eventual implementation in CAE by the industry users.

The project has successfully completed the Phase I development and has achieved the technical goals for Phase I set forth by the A/SP, which co-sponsored the work. The successful Phase I development has attracted strong support from the original equipment manufacturers (OEMs) and steel suppliers. The integrated weld process model has been licensed and transferred to industry. The SWE formulation and the Phase I results have been adopted and further refined by the OEMs and industry consortia.

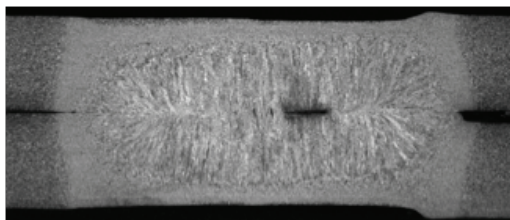
This report highlights the key developments accomplished in Phase I of the project. A comprehensive Phase I Technical Report is available that details the approaches and findings of the Phase I work.

Materials, Welding and Testing

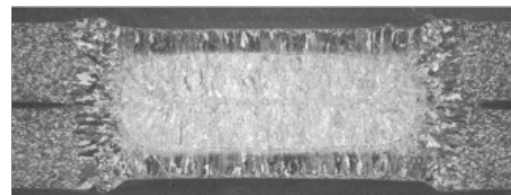
Two steels, dual-phase AHSS DP780 steel (1.15-mm thick) and DQSK mild steel (1.0-mm thick), were selected for the initial development in Phase I. DP780 was galvaneal-coated, and DQSK was hot-dip galvanized. These steels were selected and provided by the A/SP Strain Rate Characterization Committee.

For each of the steels, the welding schedule was varied to produce three different weld nugget sizes acceptable to the industry specification to study the effects of weld size on the fracture behavior of spot welds in impact testing. The welds in Phase I were made in a two-thickness (2-T) stack-up of the same steel of the same thickness.

Detailed microstructural analyses were performed to characterize the microstructure and microhardness gradients, as well as the weld defects (if any), in the weld and heat-affected zone (HAZ) of the spot welds. The microstructure and microhardness results were used to validate the weld process model for RSW. Figure 1 shows the appearance of the welds produced under different welding conditions.



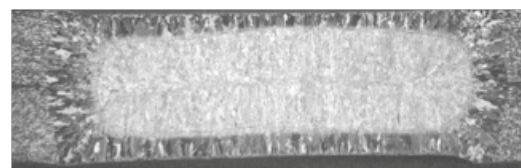
DP780 minimum nugget size



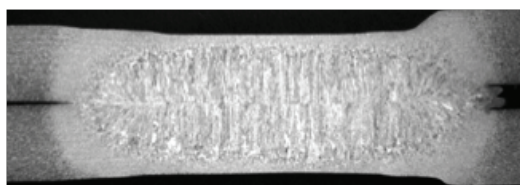
DQSK minimum nugget size



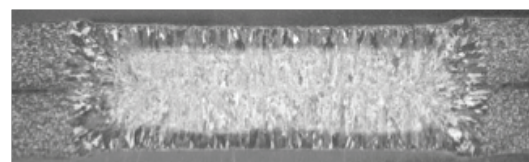
DP780 medium nugget size



DQSK medium nugget size



DP780 maximum nugget size



DQSK maximum nugget size

Figure 1. Weld nugget appearance of DP780 and DQSK welds.

Both dynamic and static testing of the spot welds, in lap-shear, cross-tension, and mixed torsion/tension loading configurations, were performed at four loading velocities: quasi-static, 2.6 m/s (5.8 mph), 3.6 m/s (8.1 mph), and 5.8 m/s (12.5 mph). The tests were carried out at University of South Carolina. A drop tower impact test machine was used for the impact tests. The fracture modes and peak loads to failure of all spot welds were analyzed. A web-based project portal and database were developed that allowed the industry members to access the project results. Dependency of the spot weld failure mode and peak load on weld size, loading mode, and loading rate were observed.

These data were used to validate the SWE modeling approach. Selected testing results are provided in Figure 2.

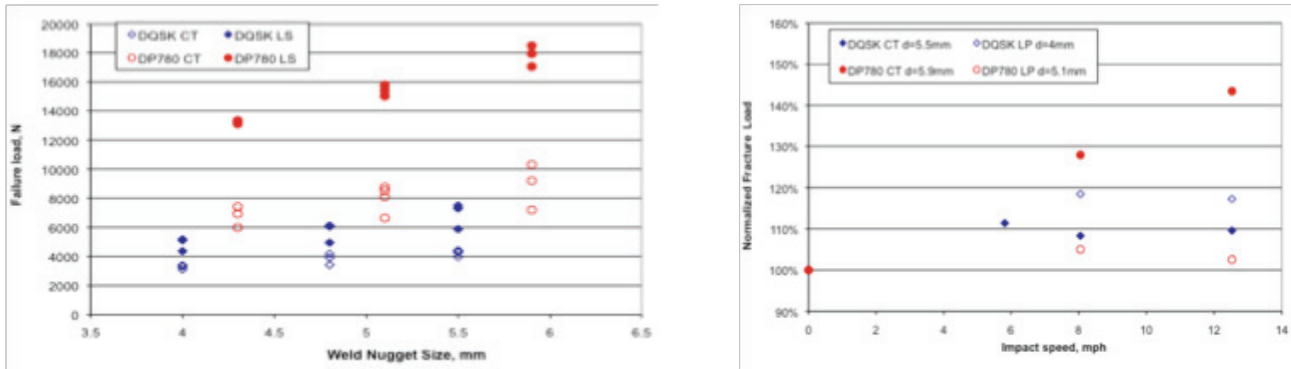


Figure 2. Effect of weld nugget size and impact speed on the fracture strength of spot welds. CT: cross-tension load, LS: lap-shear load. The fracture strength under different impact speed is normalized to the static strength of the same weld condition.

Integrated RSW Process Model

The SWE requires detailed microstructure and property information in the weld region to properly formulate the constitutive equations. An integrated electrical-thermal-mechanical-metallurgical welding process model for electric resistance spot welding was used in this project, to predict the microstructure and property gradient in the spot weld and the adjacent region. It is based on the early work with further refinement of the microstructural model for AHSS.

The integrated electrical-thermal-mechanical-metallurgical RSW process model predicts the weld size, microstructure and residual stresses in a spot weld based on the following user inputs:

- Steel chemistries and base metal microstructure
- Surface coating
- Sheet stack-ups
- Welding conditions (current and electrode force)
- Electrode geometry

A key feature of this integrated weld process model is that it predicts the microstructure evolution based on the calculations of the thermodynamics and kinetics of steel phase transformation processes. There is no need to experimentally measure the continuous cooling transformation (CCT) curves for given steel, an impossible task for all possible thermal cycles experienced in different locations of the weld and HAZ of a spot weld.

The integrated RSW process model was applied to the two steels and different welding conditions in Phase I. The simulation results compared well with the measurement results

of weld microstructure and microhardness distributions. Figure 3 shows the predicted weld nugget, volume fraction of different phases, and the resultant microhardness distributions in a DQSK spot weld. The weld nugget region exhibits a complex distribution of martensite, bainite and ferrite. The comparison of microhardness distribution of both DQSK and DP780 steels are presented in Figure 4. For each steel, the prediction is in the top contour plot, whereas the measurement results are given in the middle contour plot and also the bottom line plot along the middle thickness of the steel sheet.

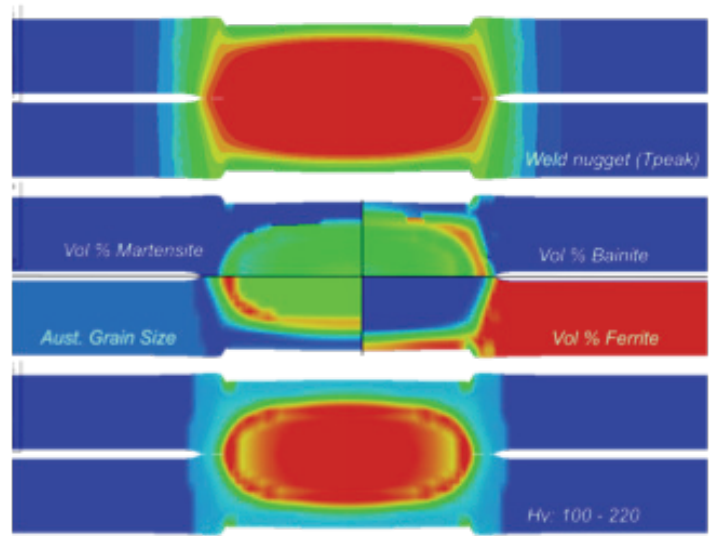


Figure 3. Predicted weld nugget as represented by the peak temperature in red color (top), volume fractions of different phases (middle), and microhardness distribution (bottom) in a DQSK spot weld.

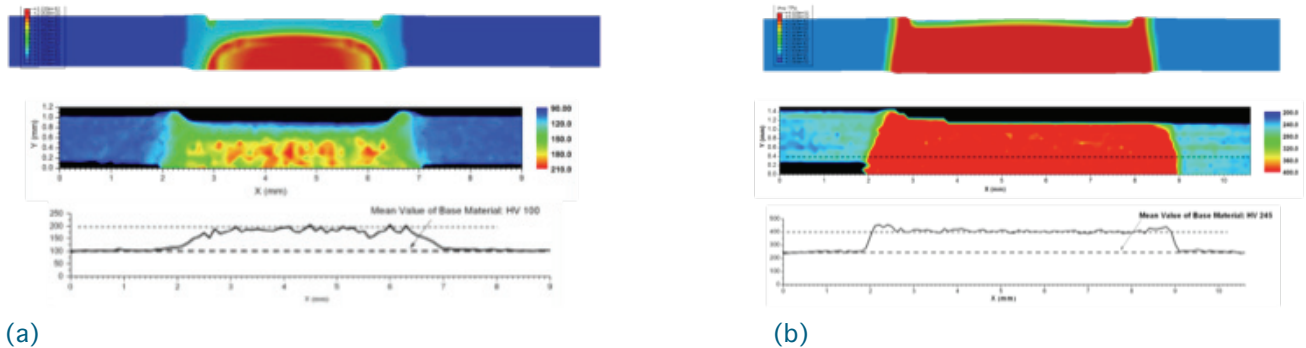


Figure 4. Microhardness distribution. (a) DQSK, (b) DP780.

Development of Spot Weld Element

Spot welds in finite-element modeling (FEM) impact simulations are usually modeled with two sub-models; a kinematics model of the joint and the associated constitutive model describing the material-related response of the joint. Currently, the kinematics of the joint is primarily modeled as point-to-point connection by means of flexible or rigid (i.e. constrained) line finite elements. The line connection restricts the constitutive spot weld models to force-based laws. This in turn requires extensive experiments to determine the model parameters for different RSW configurations (nugget size or steel chemistry, for example). One of the principal problems with beam-based kinematics models in AHSS spot welds is that the stress and strain distributions in the weld area are not accurately represented. For RSW in conventional steel structures, the dominant failure mode is the button pullout and the inadequate calculation of the shear stress may not be a major concern in impact simulation of vehicles. However, for AHSS RSW, accurate determination of the shear stress may be critical because of the occurrence of the interfacial

failure or mixed interfacial plus pullout failure mode. In addition, the multiple failure modes and the changes in failure modes under different loading conditions require development of more versatile failure criteria based on the fracture and damage mechanics principles than the resultant force-based ones. From the structural stiffness perspective, the bar and beam models typically yield acceptable accuracy under tension, out-of-plane torsion and bending loads. For in-plane torsion and shear, the stiffness values are highly inaccurate. The brittle fracture associated with the interfacial failure of the spot weld is more likely during impact where plastic deformation of the base material may be constrained by large elastic stress field. Compared to a gradual increase in hardness in the HAZ in mild steel RSWs, the AHSS exhibit sharp hardness change that adds to brittleness and notch sensitivity of the joint.

The SWE formulation developed in this project allows for more accurate representation of the stress distribution in the weld zone that is computationally feasible for crash simulations. The recent RSW models based on solid elements inserted between shell elements of the sheet material have shown much better accuracy than the line-based elements. We have extended that approach to the model configurations illustrated below in Figure 5. The schemes depict through-thickness direction of the spot weld.

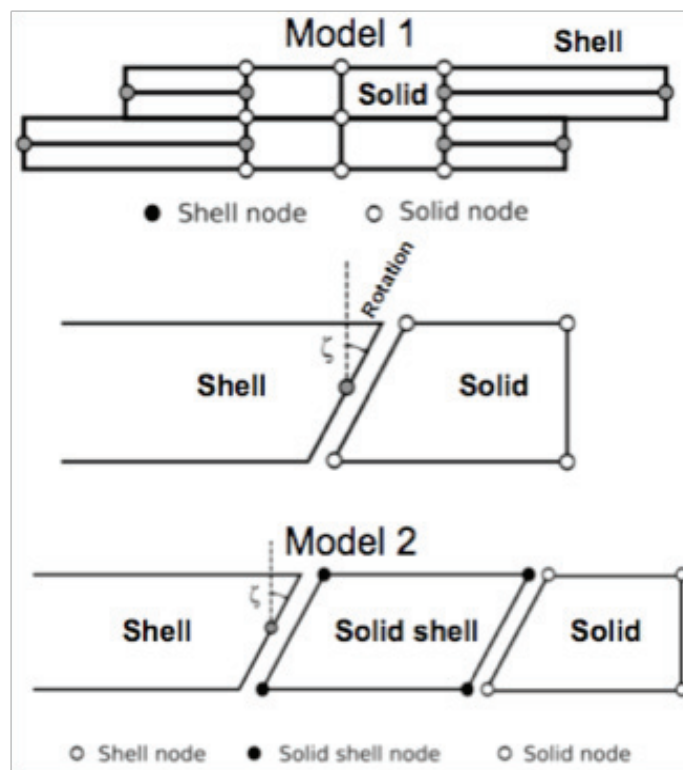


Figure 5. Configuration of the spot weld model in the through-thickness direction. Model 1 has shell elements in the HAZ and the plate whereas Model 2 used 8-node solid shell for the HAZ. The middle figure shows the coupling between the 4-node shell and solid.

The models have compatible connection between the plate (shell) and the nugget (solid) regions. The principal difficulty is the element meshing of the region, but with the current computational design tools such connections should be easily manageable. Additional simplification of the connection comes from the fact that the inner region of the spot weld is relatively stress free compared to its periphery. Accordingly, the inner region of the weld can be replaced by computationally inexpensive rigid elements, or equivalently, kinematic constraints. The constraints computationally stabilize the solid elements in the deformable region of the spot weld and provide additional mass that can be used for computational speed-up of the region using mass time scaling.

Possible failure regions in the new spot weld connection are shown in [Figure 6](#). The stress-strain values in those regions can be used to evaluate various fracture criteria that would initiate failure of the spot weld. In Phase I, a simple failure criterion based on equivalent strain to failure was used. The material properties in the weld region were based on the hardness measurements and simulations. Base material properties were scaled with the simulated/measured hardness coefficient and equivalent strain to failure was reduced accordingly. This constitutes a very simplistic model that will need to be refined by more accurate criteria in the future.

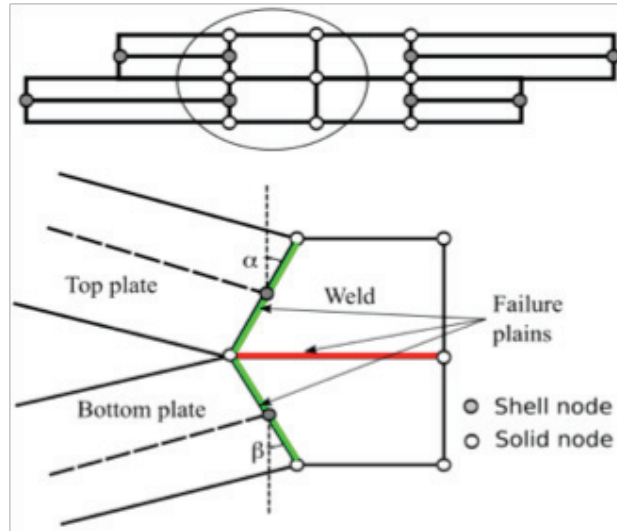


Figure 6. Failure zones in the spot weld model.

Lap-Shear Specimen Simulations

The standard lap-shear specimen geometry was simulated, with detailed FEM discretization shown in [Figure 7](#). [Figure 8](#) shows the simulation side view of the spot weld region of the lap-shear test with small nugget diameter. The figure shows configurations before and after the failure. The failure of the spot weld in simulation and experiments was along the interface between the two connected sheets.

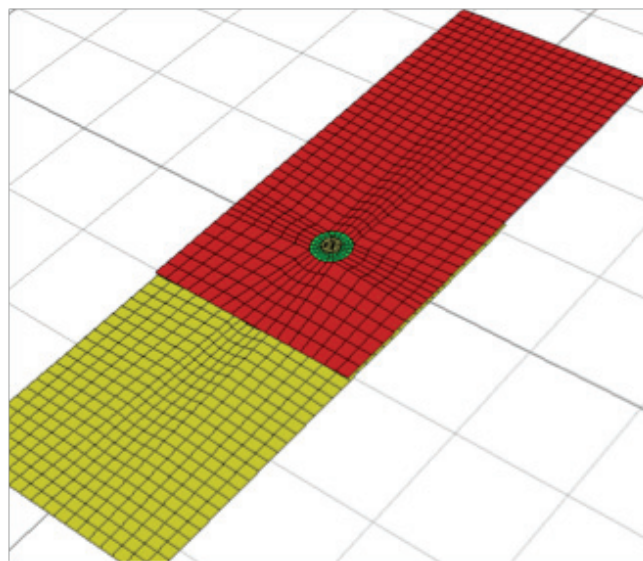


Figure 7. Lap-shear specimen model. Detailed FEM mesh.



Figure 8. Lap shear test simulation for small spot weld nugget diameter (4.3 mm). DP780 steel.

Comparison of the force-displacement data from simulation and the quasi-static test is shown in Figure 9. The resulting force comparison is very close given the experimental scatter and the simplicity of the failure model. The simulation for large spot weld diameter in lap shear test is shown in Figure 10. The simulation in Figure 11 is again reasonably close to the experimentally measured force and stiffness of the assembly.

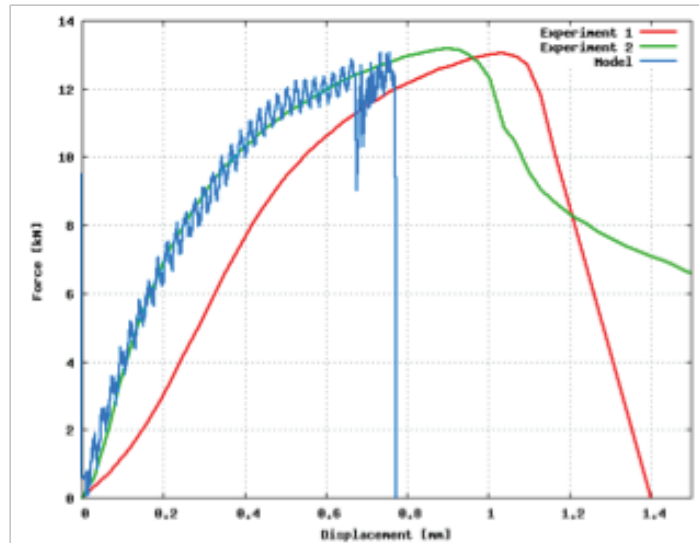


Figure 9. Comparison of the resulting force for experiments and simulations for DP780 steel, small spot weld diameter (4.3 mm).

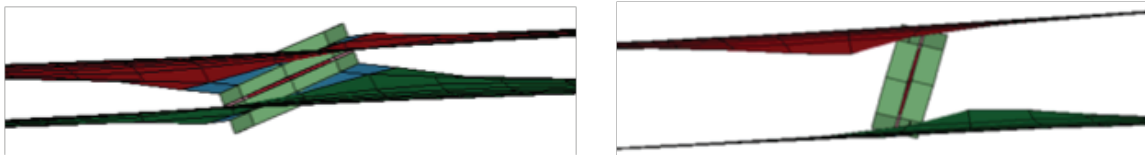


Figure 10. Lap shear test simulation for large spot weld diameter (5.9 mm).

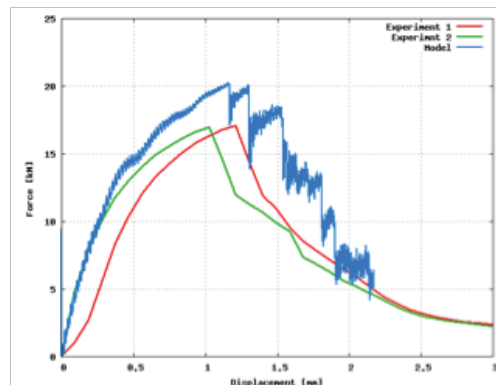


Figure 11. Comparison of the resulting force for experiments and simulations for DP780 steel, large spot weld diameter (5.9 mm).

The spot weld model accurately recovers geometry effect based on intrinsic material properties and a very simple failure condition, without a need for accounting of any extrinsic joint properties such as nugget diameter.

Cross-Tension simulations

Model geometry configuration for the cross-tension test is shown in [Figure 12](#). The clamped boundary conditions are imposed on the nodes emerging from the fixture.

Simulation of the cross-tension test of DP780 steel with large nugget diameter ($D=5.9$ mm) is shown in [Figure 13](#).

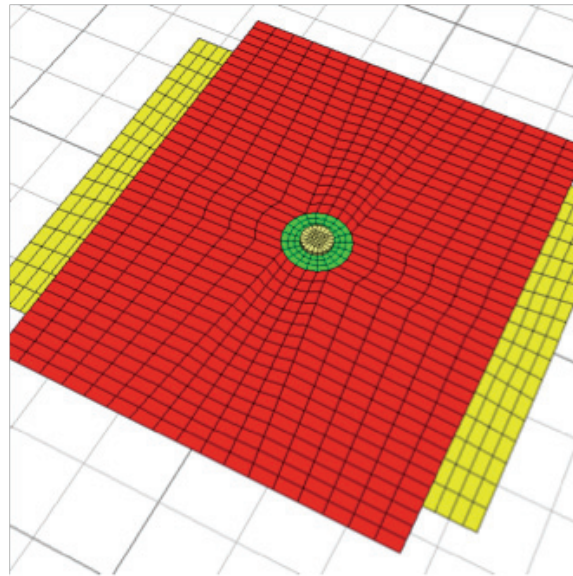


Figure 12. Geometry configuration of the cross-tension specimen. Detailed FEM discretization.

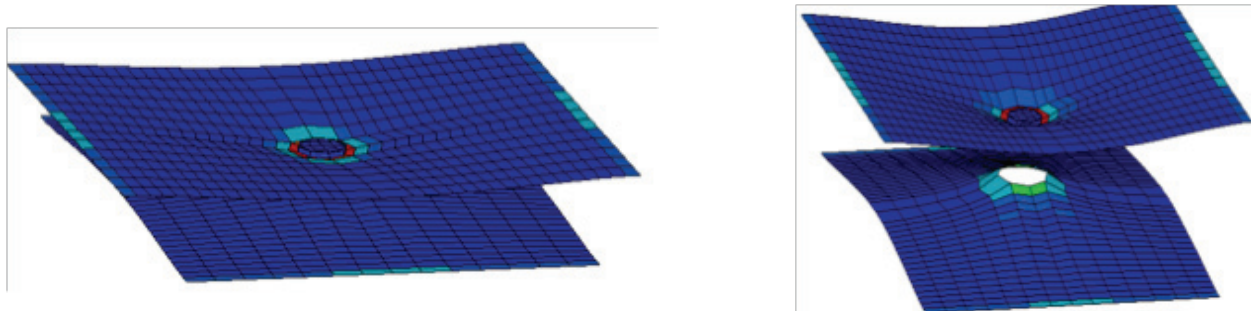


Figure 13. Cross-tension specimen deformation before and after the joint failure. DP780 steel, large spot weld diameter (5.9 mm).

When the model is compared with impact experiments, [Figure 14](#), a relatively large scatter of the results can be noted. The origin of this disparity may be in incomplete clamping in experiments, as the post-test specimen analysis showed traces of slipping in the clamps.

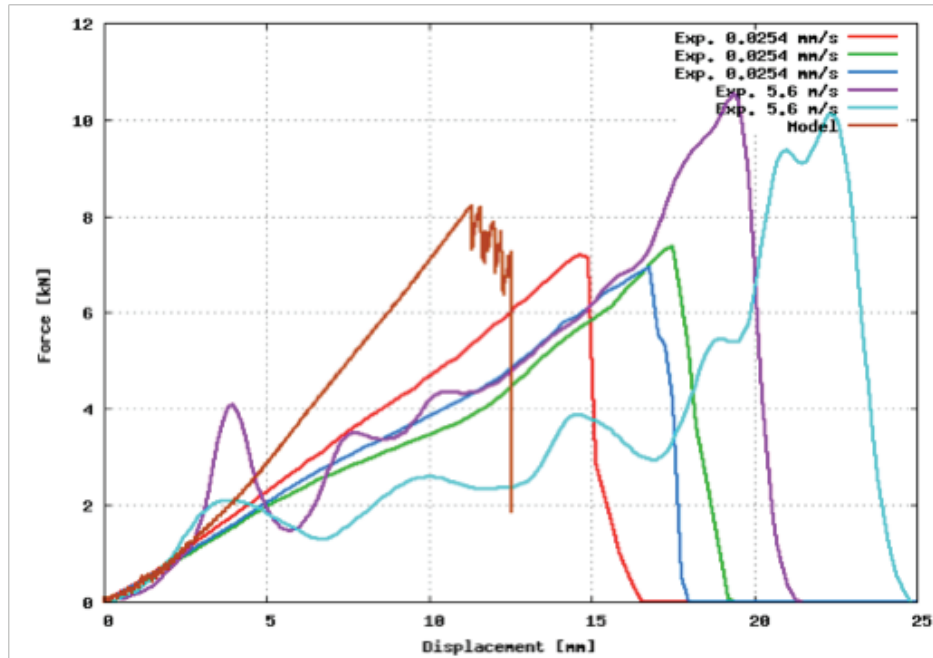


Figure 14. Comparison of the model with experiments for quasi-static and impact tests. DP780 steel, large spot weld diameter (5.9mm).

The origin of stiffer behavior may also be in the size of the shell elements in the HAZ zone. The elements in that zone are responsible for the overall failure. The actual strain localization zone is very small and we need to scale the plastic strain to failure with respect to the size of the finite elements in order to conserve the energy to failure. Normalization procedures and viscous regularization based on strain rate effects can be employed for this purpose. Overall, maximum force in the simulation corresponds very well to the tests.

Conclusions

Phase I (concept feasibility) of the project successfully carried out the initial development of the Spot Weld Element (SWE) modeling framework and demonstration of the effectiveness of such a modeling approach. Specifically,

- The initial version of SWE has been developed with the following capabilities:
 1. Capable of handling weld geometry and weld property gradient, and
 2. Capable of predicting different fracture modes and fracture load limit experimentally observed in impact tests.
- The initial version of integrated electrical-thermal-mechanical-metallurgical resistance spot weld model has been developed with the following capabilities:
 1. Capable of predicting weld geometry, microstructure and microhardness distributions, and
 2. Friendly user input interface for welding parameters, sheet thickness and steel chemistry.
- Baseline spot weld impact test data on DP780 and DQSK steels have been collected and analyzed to characterize the effects of impact speeds and loading modes, and
- A web-based database has been set-up for user-friendly interactive data analysis and retrieval.

Acknowledgement

The authors acknowledge with gratitude the technical guidance of the Auto/Steel Partnership Strain Rate Characterization Project Team, especially of the technical contributions of the following members: Dr. Kathy Wang (Chair, General Motors), Dr. Dave Muelemen (past Chair, General Motors), Omar Farugue (Ford), Tau Tyan (Ford), J. Z. Cao (Chrysler), Ilaria Accorsi (Chrysler), Vinod Makam (Chrysler), Ming Chen (U.S. Steel), Min Kou (ArcelorMittal), Raj Mohan lyengar (Severstal N.A.) and Pat Villano (Auto/Steel Partnership). Experimental data were provided by Dr. Y.J. (Bill) Chao and Y. Kim of University of South Carolina under a companion project sponsored by the Auto/Steel Partnership.

Presentations/Publications/Patents

Feng, Z., Simunovic, S. Chao. B, Wang, K., Belwafa, J. and Chen, M.; "Impact Modeling and Characterization of Spot Welds," International Auto Body Congress (IABC) 2009, Nov 4-5, 2009, Troy, MI.

C. Friction Stir Spot Welding of Advanced High Strength Steels

Principal Investigator: Michael L. Santella
Oak Ridge National Laboratory
1 Bethel Valley Road, Oak Ridge, TN 37831-6096
(865) 574-4805; e-mail: santellaml@ornl.gov

Principal Investigator: Glenn J. Grant
Pacific Northwest National Laboratory
902 Battelle Boulevard, P.O. Box 999, Richland, WA 99352
(509) 375-6890; e-mail: Glenn.Grant@pnl.gov

Principal Investigator: Yuri Hovanski
Pacific Northwest National Laboratory
902 Battelle Boulevard, P.O. Box 999, Richland, WA 99352
(509) 375-3940; e-mail: Yuri.Hovanski@pnl.gov

Technology Area Development Manager: Dr. Carol Schutte
(202) 287-5371; e-mail: carol.schutte@ee.doe.gov

Field Technical Co-Manager: C. David Warren
(865) 574-9693; e-mail: warrencd@ornl.gov

Field Technical Co-Manager: Mark Smith
(509) 375-4478; e-mail: mark.smith@pnl.gov

Contractor: Oak Ridge National Laboratory & Pacific Northwest National Laboratory
Contract No.: DE-AC05-00OR22725 & DE-AC06-76RLO1830

Objective

- The overall objective of this project is to develop friction stir spot welding (FSSW) as a superior method to join Advanced High Strength Steels (AHSS).
- Specific objectives of Phase 1 activities were to address the critical questions of whether there are tool materials available that have potential for reasonable life, and whether FSSWs made in AHSS are feasible and can develop similar or better mechanical performance than welds made by conventional processes like resistance spot welding (RSW).
- Specific objectives of Phase 2 activities were to increase joint strengths and minimize welding cycle times through systematic investigations into weld process parameters, and to further examine the effects of tool designs and tool materials on joint properties and processing requirements.

Approach

- The project is collaboration between ORNL and PNNL, and includes a committee of consultants from Chrysler Group LLC, Ford Motor Company, General Motors Company (GM), several steel manufacturers and a friction stir tool manufacturer.

- Lap-joints were made and used to correlate tensile-shear strength with processing parameters and microstructures.

Milestones, Metrics and Accomplishments

- Hundreds (> 600) of friction stir spot welds were made on uncoated dual-phase sheet steel with nominal tensile strength of 780 MPa (DP780), galvanized DP780 (DP780GA), and uncoated hot-stamp boron steel (HSB steel, or HSBS) using a wide range of welding conditions.
- Strength data were accumulated on the effects of weld time, tool rotation speed, and tool shape on weld appearance, bonding, fracture, microstructures, properties, and process loads.
- Mechanical testing of Phase 1 lap shear coupons in DP780 and HSBS indicated that while overall strengths for certain weld parameters were in the range of acceptable values defined by the American Welding Society (AWS) Specification for RSW of steel, the specific strength of nearly any condition exceeded the minimum stress condition.
- Mechanical testing of friction stir spot welds made with Phase 2 tools produced dramatic increases in lap-shear strength when compared to the results from welds produced with Phase 1 tools.
- For weld times of 4 seconds, the maximum lap-shear tensile strengths measured were 17 kN for DP780, 22 kN for galvanized DP780, and 16 kN for hot-stamp boron steel. All of these values exceeded minimums specified in the AWS Specification for RSW.
- Lap-shear strengths tended to increase with removal of mill finishes indicating that surface conditions of the sheets influenced mechanical properties and bonding.
- For otherwise identical welding conditions, increasing tool rotation speed from 800 to 1600 revolutions per minute (rpm) increased strength values for spot welds made with DP780 and DP780GA. Using a 2-step schedule rather than a 1-step schedule had a similar effect. Metallographic examinations indicated this was related to increased bonded area.
- Stir tools of six different tool materials were made and evaluated. These materials were tungsten 25% rhenium alloy, polycrystalline boron nitride (PCBN), silicon nitride, titanium diboride, tungsten carbide-cobalt, and a cermet made of complex carbides bonded by a refractory metal alloy.
- PCBN demonstrated the most promise as a stir tool. Wear rates in PCBN tools were very low, although the overall durability, availability and cost are concerns for widespread commercial applicability.
- Results also confirmed that tool shape has a significant influence on lap-shear strength.

Future Direction

The primary objective of the continuing project is to evaluate friction stir spot welding (FSSW) on steels strengthened by transformation-induced plasticity (TRIP steels), and any others for which cost-effective joining solutions are not already available as identified by industry representatives. Compared to previous work, the overall approach will involve:

- More comprehensive characterization of mechanical behavior including fatigue strength, T-peel strength, cross-tension strength, possibly impact behavior, and metallurgical examinations

- Identification and characterization of liquid metal embrittlement phenomena
- Concentrated evaluation of candidate materials for friction stir tools
- Interaction with equipment suppliers to so that their constraints help guide decisions about welding parameters and tooling.

Introduction

The technology for implementing Friction Stir Spot Welding (FSSW) of aluminum in automotive manufacturing environments exists. C-gun-type FSSW heads have been developed and adapted to robotic systems that are now commercially available for FSSW of aluminum alloys. This project addresses the questions of whether the FSSW process is viable for joining Advanced High Strength Steels (AHSS) and whether FSSW has advantages over conventional processes like resistance spot welding (RSW). Preliminary work on FSSW of AHSS suggested that several features of the process (fine grained microstructure in the nuggets of AHSS, potentially higher strength joints, higher energy absorption in crash, low energy consumption and environmental emission reduction during manufacturing) may give FSSW cost and energy saving advantages over RSW. In addition, the process may be viable for high-strength, lightweighting alloys that currently have joining problems using conventional techniques (DP1000, martensitic steels such as hot-stamp boron steels, etc.).

Important questions remain about effective, economical application of FSSW to certain AHSS alloys like TRIP steels. Critical questions being addressed in this continuing work include:

- More comprehensive characterization of mechanical behavior including fatigue strength, T-peel strength, cross-tension strength, possibly impact behavior, and metallurgical examinations.
- Identification and characterization of liquid metal embrittlement phenomena.
- Development of a consensus approach for comparing FSSW joints to those made by other processes such as resistance spot welding, clinching, and adhesive bonding.
- Concentrated evaluation of candidate materials for friction stir tools.
- Interaction with equipment suppliers to so that their constraints help guide decisions about welding parameters and tooling.

If the effectiveness of FSSW for joining AHSS is established, this could accelerate the insertion of these high-strength lightweighting alloys into automotive body construction to help meet FreedomCAR goals.

Approach

The primary objective of this project is to characterize the responses of advanced high-strength steels to FSSW. The project was organized into two phases. Phase 1 activities addressed the critical questions of whether there are tool materials available that have the potential for reasonable life and whether FSSWs made in high strength steels could develop strengths comparable to those made by conventional processes like RSW. Phase 2 emphasized some of the factors crucial to industrial implementation of FSSW, concentrating on issues of weld cycle time, tool durability, process robustness and repeatability. The Phase 1 results combined with the initial work under Phase 2 highlighted two important challenges: the need for robust economical tool materials, and the complexities of developing welding parameters capable of consistently producing high joint strengths.

Presently, PCBN is the most durable, effective material from which to make stir tools for welding of steels. PCBN is relatively expensive. It is also difficult to machine into the needed shapes, and it is not widely available for purchase. These characteristics significantly complicate modifying tool designs, but such modification is a critical element of maximizing joint strengths. In addition, the intrinsic durability of PCBN is not well characterized. There is considerable interest in identifying and evaluating alternatives to PCBN, particularly any that would reduce tool costs and improve durability.

Relative to the second set of challenges, joint strengths are being obtained that compare favorably with minimum values specified in industry standards for spot welds such as AWS D8.1M. However, the consistency of obtaining these strength levels must be improved. In addition, welding times must be minimized. These conditions can be met by increasing the bonded area of FSSWs. Clearly, both sets of issues, those related to tooling and those related to joint strength, are themselves interrelated. Besides addressing the issues discussed above, Phase 2 encompassed evaluating joint microstructures and mechanical properties, and establishing a framework of a design database for spot friction welded structures.

The project is a 50/50 collaboration between Oak Ridge National Laboratory (ORNL) and Pacific Northwest National Laboratory (PNNL). Additionally, it includes a panel of consultants including representatives from Chrysler, Ford, and GM, and at various other times, representatives of ArcelorMittal, Gestamp US Hardtech, Inc., and MegaStir.

Experimental Details and Results

Materials and Experimental Details

The bulk of this work was done using two uncoated high-strength steels: the dual-phased steel, DP780, and a hot-stamp boron steel (HSBS), (sourced from a Swedish supplier, the parent of US Hardtech). The DP780 is 1.5-mm-thick sheet; the thickness of the HSB steel is 1.4 mm. More recently, a lot of galvanized DP780 (U.S. Steel) was included in the program. The nominal thickness of this sheet was also 1.5 mm. The suffix, GA, is added to specifically identify this steel and results obtained with it. In very recent times, some exploratory welds were made on TRIP steel provided by GM.

Most of the FSSW done during Phase 1 and Phase 2 was with PCBN tools. However, during Phase 2, several new tool materials were evaluated including, silicon nitride (Si_3N_4), titanium diboride (TiB_2) and new tungsten-based cermet alloys. The Si_3N_4 is still currently under investigation as a lower cost alternative to PCBN.

All spot welds are made in displacement-control mode by varying the parameters of tool plunge depth and tool plunging rate. In addition to these control parameters, a number of other process variables are typically recorded for each weld including weld time, spindle torque, normal force, and temperature on the back side of the two-sheet stack-ups. This additional information is archived for future use and analysis.

Joint strength is evaluated by tension testing lap joints to determine their shear-tension strengths. Strengths are correlated with processing parameters and microstructures. Microhardness mapping is also being used to assess the characteristics and properties of the joints.

Joint Strength Testing

Several sets of welds were made for additional testing. An offer was received from Ford Scientific Research Laboratories to conduct fatigue tests of FSSWs made on this project. One set of 15 welds each was supplied for DP780 and the HSB steel. All of the welds were made with the BN46 tool using, the 2-step procedure, and 1600 rpm. These are the conditions that produced the highest lap-shear strengths. Unfortunately, the Ford staff who offered to run these tests was terminated in a round of downsizing. The specimen could not be recovered, so these tests were not completed.

A similar welding strategy was used to make specimens for initial cross-weld tension testing and the DP780GA steel was also included. Welds were also made with the BN77 tool. Five welds were made for each tool/steel combination and the results are shown in [Table 1](#).

Table 1. Results of initial cross-tension testing (5 specimens for each combination).

Steel-Tool	Max. load, kN	Std. Dev., kN
DP780-BN77	4.34	0.21
DP780-BN46	3.43	0.47
DP780GA-BN77	4.73	0.64
DP780GA-BN46	2.15	0.16
HSBS-BN77	4.17	0.81
HSBS-BN46	1.98	0.24

The cross tension strengths were not conclusively related to base metal strength, but may be used as an indication of weld strength. The AWS standard D8.1 recommends a minimum cross tension strength of 3 kN for material that is nominally 1.5 mm thick. The data presented in [Table 1](#) indicate that all the welds made with the BN77 tool exceeded 3 kN. They also had higher strengths than those made with the BN46 tool. This is the reverse of the results found during lap-shear tension testing.

Impact of Tooling Costs on Process Economics

Working through our industry collaborators enabled the FSSW process costs to be compared to those of RSW. The analysis was based on the following welding details:

- Comparison was based on an existing component requiring 46 spot welds to build.
- Welding involved 3 pedestal welding stations making 23 welds, and 3 robotic stations making 23 welds.
- Annual production volume was 320,000 requiring a total of 14,720,000 welds/year.
- Production rate was 85 components/hour.
- Assumed energy consumption was 2.1 W-h/weld for FSSW and 3.9 W-h/weld for RSW.
- The same teardown criteria were used for both processes.

There was no assumption of existing equipment, so both installations were completely new. This resulted in equipment costs for FSSW being about 10% lower than those for RSW. Additionally, utility costs for FSSW were assumed to be only about 30% of those required for RSW. Most other costs such as those of floor space charges, utility infrastructure, direct and indirect labor, and inspection were similar for the two processes. Costs for maintenance and downtime were dependent on welding tip/tool life. These were the major cost differences for the two processes. For RSW, the cost of welding electrodes was assumed to be \$0.65/tip, and the assumed tip life was 5000 welds. For FSSW, stir tools were assumed to cost \$100, \$300, \$500, or \$2,000.

Collectively, these assumptions were then used to estimate the variation of process costs with stir tool life. A premium in cost was found for FSSW and this is illustrated graphically in Figure 1.

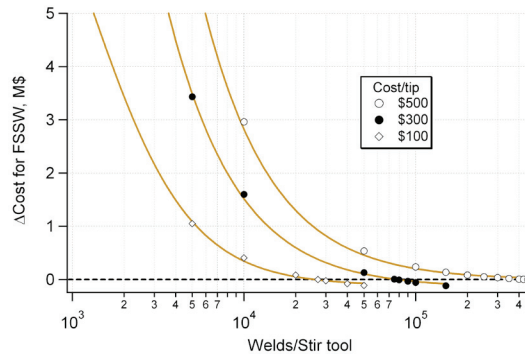


Figure 1. Variations of cost of FSSW relative to RSW depending on stir tool cost and life.

This analysis indicates that at \$100/tool, stir tools would need to survive for about 26,000 welds to be cost neutral relative to RSW. Higher stir tool costs demand significantly higher lives to meet the same criterion. The cost of tools being used in current experimental work is \$2,500-3,000. No systematic evaluation of tool durability has been done yet, but experience on this project suggests that PCBN tool life is likely to be on the order of 500-1,000 welds. Consequently, reducing the cost of tooling appears to be a significant challenge if FSSW is to compete directly with RSW. Alternatively, at current tool prices there must be compelling technical reasons to use FSSW rather than RSW.

Initial Evaluation of FSSW of TRIP Steel

Several series of spot welds were made using a 1.5-mm-thick TRIP steel provided by GM. The steel was reported to be uncoated. The stir tools used for these welds included existing designs of PCBN as well as newly acquired tools manufactured from Si₃N₄. As for previous evaluations, welds were made using both 1-step and 2-step procedures, and tool rotation speeds of 800 and 1600 rpm. The welding time was fixed at 4 s so that strength results could be compared with existing datasets. The various welding details and lap-shear strength results are presented in Table 2.

Table 2. Initial results for FSSW of uncoated TRIP steel.

Tooling	rpm	Steps	kN
BN97	800	1	9.7
	1600	1	11.3
	1600	2	15.1
BN46	1600	1	8.1
	1600	2	12.5
SN77	1600	1	6.14
SN97	1600	2	5.3

A total of five spot welds were made for each condition. Four of the welds were tested for lap-shear strength and one was reserved for metallographic analysis. The strength values in Table 2 represent averages for the 4 specimens. The BN tools are made of PCBN; the SN tools are made of Si₃N₄. This TRIP steel had a nominal strength of 780 MPa; thus, the BN97 welds at 1600 rpm and the two step BN46 welds exceeded AWS D8.1 minimum values.

Conclusions

1. Sets of 15 welds each were made with the HSB steel and DP780 using a 2-step welding schedule and the BN46 tool. These were provided to the Ford Scientific Research Laboratory for fatigue testing.
2. Cross tension testing indicated that welds made with the BN77 tool had higher strengths than welds made with the BN46 tool.
3. An economic analysis suggested that either stir tool prices must reduce significantly or tool life must increase significantly for FSSW to be cost-competitive with RSW for automobile assembly operations.
4. Initial testing of FSSWs made with an uncoated TRIP780 steel indicate they are capable of exceeding minimum values required of resistance spot welds.

Presentations/Publications/Patents

1. Y. Hovanski, M.L. Santella and G.J. Grant. Friction Stir Spot Welding of Hot-Stamped Boron Steel. *Scripta Materialia*, 57 (2007) 873-876
2. Y. Hovanski, M.L. Santella and G.J. Grant. Friction stir spot welding of advanced high strength steels. Presentation at MS&T Sept. 2007
3. G.J. Grant, Y. Hovanski, and M.L. Santella, Friction Stir Spot Welding of Advanced High Strength Steels for Automotive Applications In: International Symposium on Friction-based Spot Welding Processes, eds. A.M da Silva, J.F.dos Santos, G. Amancio, International Institute of Welding, GKSS Forschungszentrum, Geesthacht, Germany, 2007, pp107-148
4. M.L. Santella, A. Frederick, Y. Hovanski, and G.J. Grant, Friction Stir Spot Welding of DP780 and Hot-Stamp Boron Steels, published in Proceedings of Sheet Metal Welding Conference XIII, American Welding Society, 2008
5. M.L. Santella, A. Frederick, Y. Hovanski, and G.J. Grant, Friction Stir Spot Welding of DP780 and Hot-Stamp Boron Steels, presented at Sheet Metal Welding Conference XIII, Livonia, Michigan, May 16, 2008
6. Y. Hovanski, M.L. Santella and G.J. Grant. Friction Stir Spot Welding of Advanced High Strength Steels, Presentation at MS&T Sept. 2008
7. Y. Hovanski, M.L. Santella, and G.J. Grant, Friction Stir Spot Welding of Advanced High Strength Steels, presented and published in conference proceedings of Friction Stir Welding and Processing-V, TMS, 2009
8. M.L. Santella, Y. Hovanski, A. Frederick, G.J. Grant, and M.E. Dahl, Friction Stir Spot Welding of DP780 Carbon Steel, accepted for publication in Science and Technology of Welding and Joining, October, 2009
9. Y. Hovanski, M.L. Santella and G.J. Grant. Friction Stir Spot Welding of Advanced High Strength Steels, Presentation at MS&T Oct. 2009
10. Y. Hovanski, M.L. Santella and G.J. Grant. Friction Stir Spot Welding of Advanced High Strength Steels, Presentation at IABC, Troy, MI, Nov. 2009
11. Y. Hovanski, M.L. Santella and G.J. Grant. Friction Stir Spot Welding of Advanced High Strength Steels, published in conference proceedings of IABC 2009, IABC, Troy, MI, Nov. 2009

D. Friction Stir & Ultrasonic Solid State Joining Magnesium to Steel

Principal Investigators: Glenn J. Grant, Yuri Hovanski
Pacific Northwest National Laboratory
902 Battelle Blvd.; P.O. Box 999, Richland, WA 99352
(509) 375-6890; e-mail: glenn.grant@pnl.gov
(509) 375-3940; e-mail: yuri.hovanski@pnl.gov

Principal Investigator: Michael L. Santella
Oak Ridge National Laboratory
1 Bethel Valley Rd.; Oak Ridge, TN 37831-6096
(865) 574-4805; e-mail: santellaml@ornl.gov

Industry Consultants: Elizabeth Hetrick - Ford; James F. Quinn and Blair Carlson - General Motors;
and Joe Beckham - Chrysler

Technology Area Development Manager: William Joost
(202) 287-6020; e-mail: liam.joost@ee.doe.gov

Field Technical Managers: C. David Warren, Mark T. Smith
(865) 574-9693; e-mail: warrencd@ornl.gov
(509) 375-4478; e-mail: mark.smith@pnl.gov

Contractor: Oak Ridge National Laboratory & Pacific Northwest National Laboratory
Contract Nos.: DE-AC05-00OR22725 & DE-AC05-76RL01830

Objective

- Establish the applied technical understanding necessary to produce robust joints between magnesium alloys and steel using solid state joining, friction stir welding (FSW) and ultrasonics.
- Develop the fundamental relationships influencing bond formation in metallurgical, mechanical and chemical forms created during FSW and ultrasonic welding (USW) solid state processes. Ascertain their responses to changing alloys, product forms and surface conditions as they affect creation of structural joints between magnesium and steel.
- Determine the effect of FSW and ultrasonic joining on corrosion protection coatings and characterize the corrosion performance of joined assemblies.

Approach

- Systematically evaluate the application of friction stir and ultrasonic processes to welding of magnesium to steel. Develop an improved understanding of the interaction of each unique energy source with appropriate alloy/product form combinations as agreed upon by our industrial advisors.
- Investigate the fundamental aspects of bond formation (metallurgical and/or mechanical) during the solid state process and investigate the response to changing alloys, product forms (wrought, castings) and surface conditions (coatings).

- The materials being joined (magnesium and steel) form a strong galvanic couple. Strategies to prevent corrosion in the joint, including potentially unbroken interlayers or transition materials, complete encapsulation, coatings or hermetic adhesives that are welded through during the joining process will be employed to mitigate the potential for galvanic coupling.

Milestones, Metrics, and Accomplishments

- Milestone 1 (Task 1): Demonstrate solid-state joining of magnesium to steel achieving strengths of 1.0 kiloNewtons (kN) times the thickness of the thinner material (or 40% joint efficiency) in the dissimilar combination. Linear and spot welds were prepared using FSW and USW, respectively. Lap shear tensile tests were performed showing spot welds strengths in excess of 2.6 kN and linear friction stir welded joints with joint efficiencies in excess of 50% based on the tensile strength of the steel sheet material (completed June 2009).
- Milestone 2.1 (Task 2): Complete baseline structural joints between magnesium to steel achieving strengths of 1.5 kN times the thickness of the thinner material (or 60% joint efficiency) in the dissimilar combination. Tensile tests were again performed on magnesium/steel lap shear joints showing spot weld strengths in excess of 4 kN. Lap shear strengths of linear friction stir welds ranged between 40% and 80% depending on the material combination (completed September 2009).
- Developed introductory experimental design parameters for magnesium to steel joints using both friction stir and ultrasonic welding techniques.
- Fabricated initial tooling and fixtures required for both solid-state techniques under investigation.
- Procured and received initial materials in several of the applicable alloy forms and gauges to begin testing. Coordinated with the Magnesium Front End Research and Development group to obtain materials in support of dissimilar joining goals.
- Completed initial milestones demonstrating the ability to effectively join magnesium to steel using both FSW and USW solid-state techniques.
- Completed initial investigation into bond formation and performance of magnesium to steel joints, including x-ray diffraction analysis to determine the compositions of the interlayer formed during the joining process.

Future Direction

- Milestone 2.5 (Task 2): Complete investigation into bond formation and performance as a function of joining parameters.
- Milestone 2.3 and 2.4 (Task 2): Complete joining experiments in both FSW and USW demonstrating parameters for achieving 75% joint efficiency (or 2.0 kN times the thickness of the thinner material).
- Develop an improved understanding of the interaction of the energy source with appropriate alloy/product form combinations in FSW. Factors affecting joint strength will include tool design, process speed and feed and pin design and location relative to interface.
- Continue investigation of alternative sonotrode tip materials, including in-depth examination of tooling/steel interactions.

- Distribute technical reports to original equipment manufacturers (OEMs) documenting the joining parameters, material properties tables and corrosion potentials for joints between subject magnesium and steel alloys.

Introduction

Decreasing automobile weight can directly contribute to reducing fuel consumption. Increasing the use of lightweight materials and implementing manufacturing technologies that enable the use of lightweight materials are the two primary paths toward weight reduction. In some situations, lightweight materials can be directly substituted for higher density materials, but there are barriers to direct substitution. In a modern multi-material vehicle, lightweight materials such as aluminum (Al) and magnesium (Mg) alloys can be a challenge to attach to underlying substructure, which is usually composed of steel. Even in aluminum- and magnesium-intensive designs where entire substructures may be constructed of lightweight metals, there remains a need to join the substructure with other parts of the body-in-white such as the predominantly steel passenger safety cage. Joining methodologies available in the cost environment relevant to automotive manufacturing include resistance spot welding, adhesives, linear fusion welding, hemming, clinching, bolting and riveting. However, because of the highly dissimilar natures of the materials, magnesium/steel joints are extremely problematic. Magnesium-to-steel joints cannot be simply fusion welded because of the extreme differences in their melt temperatures, and joining methods that require a large amount of plastic strain in the magnesium component suffer from magnesium's poor ductility at room temperature.

As alternative joining methodologies, friction stir welding (FSW), friction stir spot welding (FSSW) and ultrasonic welding (USW) may be able to overcome traditional barriers to join and construct hybrid magnesium/steel components. These solid state joining methods provide unique joining capabilities that, if realized, may potentially produce faster and more economical alternatives to current technologies (bolting/riveting). However, FSW and USW for dissimilar magnesium/steel combination are significantly underdeveloped for broad deployment.

The purpose of this project is to develop an applied understanding of the following:

- Localized metal forming and potential metallurgical bonding that develops during FSW, FSSW, and USW
- The influence of process parameters on joint strength and performance
- The interaction of both joining processes with existing corrosion protection methods and their corrosion performance.

Approach

While the potential for using solid state joining processes such as FSW and USW to overcome the traditional difficulties associated with joining magnesium to steel is emerging, many challenges remain. Insufficient understanding of the proper processing conditions required to achieve robust joints has hampered any comprehensive evaluation of performance (strength, fatigue, durability, crash performance). Minimal existing research has yet to evaluate feasible joint geometries, and no emphasis on employing the benefits of solid state technologies in mitigating the galvanic corrosion in magnesium/steel joints has been evaluated.

This project is designed to overcome many of these technical barriers by performing three primary tasks. Task 1 was focused on systematically evaluating the application of friction stir and ultrasonic processes to the welding of magnesium to steel in a lap configuration. The work included developing an improved understanding of the interaction of each unique energy

source with appropriate alloy/product form combinations and is intended to provide a baseline conceptual feasibility for the remaining work.

After Task 1 was completed successfully, Task 2 has been focused on investigating the fundamental aspects of bond formation (metallurgical and/or mechanical) during the solid state process. This phase of the project also includes an investigation into the response to material variation caused by changing alloys, product forms (wrought, castings) and surface conditions (coatings). This task allows for further investigation of favorable methodologies outlined during the concept feasibility phase with the potential of further increasing joint strength.

Task 3 will focus on investigating strategies to prevent corrosion in the joint. This will include evaluating the effects of potentially unbroken interlayers or transition materials as well as coatings or hermetic adhesives that are welded through during the joining process. These tasks and associated deliverables are intended to enable a broader application of solid state joining technologies while further facilitating the joining of magnesium to steel.

Materials and Experimental Details

As the solid-state joining technologies evaluated herein are completely different, unique hardware is being used for the development of each joining process. Friction stir welding is being developed using a high-stiffness precision friction stir welding machine located at Pacific Northwest National Laboratory (PNNL; [Figure 1](#)), while a 2500 Watt research scale ultrasonic test frame (shown in [Figure 2](#)) is being used in the development of ultrasonic welding techniques at the Oak Ridge National Laboratory (ORNL).



Figure 1. Precision FSW machine located at PNNL



Figure 2. USW machine located at ORNL

Friction Stir Welding

Friction stir joints between magnesium and steel are produced in lap configurations with the magnesium located on the tool side of the joint. FSW tools are plunged through the thickness of the magnesium to the interface of the two materials and are subsequently translated at depth for a predetermined length. Various techniques have been designed to promote the joining characteristics of the interface, including tools that beneficially disturb the steel surface, creating clinch points or rough surfaces for the locally plasticized magnesium to adhere.

As a means of using previous research performed in FSW of Al to steel and Mg to Mg, several tool designs and materials were chosen at the onset of the project. Generally, high-carbon steels have proven to produce higher joint strengths for FSW of Mg alloys, so H-13 and MP159 tool materials were selected for initial tool production. FSW tools were produced with both pin and shoulder features to facilitate movement of the magnesium material while minimizing the peak temperatures during the FSW process.

In accordance with Task 1, a systematic evaluation of FSW of Mg to steel (Fe) was undertaken. The most promising initial results demonstrated that lap shear strengths between 2-mm-thick AZ31 Mg sheet and 1-mm galvanized drawing quality (DQGA) steel sheet exceeded 6 kiloNewtons (kN). The joint efficiency of the linear friction stir welded joint shown in Figure 3 was 59% based on the ultimate strength of the steel sheet.

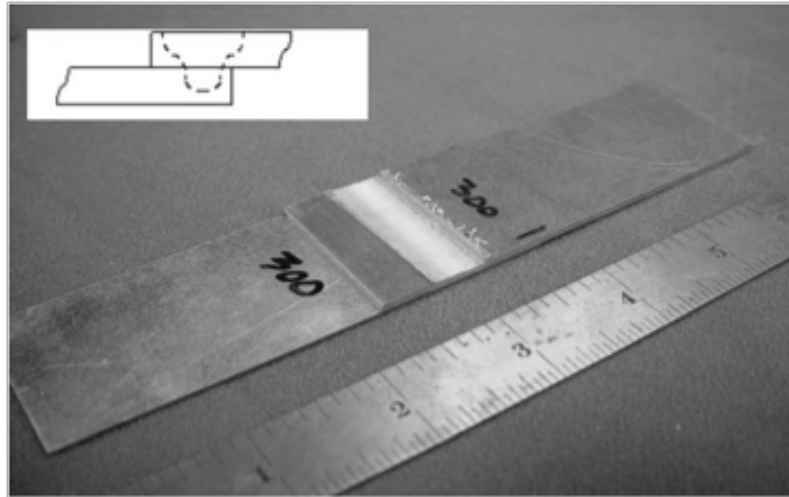


Figure 3. FSW Lap Joint between 2 mm AZ31 (top) and 1 mm DQGA (bottom)

An initial investigation into the nature of the friction stir welded joint using optical and scanning electron microscopy (SEM) microscopy as well as X-ray diffraction techniques provided insight into the bonding mechanisms between these two metals. No specific reactions were found between the Mg and Fe, yet the zinc (Zn)-based coating on the DQGA sheet showed significant reactivity with the AZ31 sheet.

Task 2 was designed to provide a greater understanding of the joint interface while simultaneously developing parameters that achieved better mechanical properties than those achieved during the first task. As such two different automotive sheet steels were used for comparative evaluation of the dissimilar joining potential. A single FSW tool design was used for both dissimilar welds, and process parameters were kept the same. Lap-shear tests indicate ~80% joint efficiency in AZ31-0.8-mm steel welds as shown in Figure 4. However, joint efficiency of AZ31-1.5-mm high strength low alloy (HSLA) steel weld was notably less (shown in Figure 5), even though the actual lap shear loads were similar. Higher joint efficiency observed in 0.8-mm steel was attributed to increased bonded area. Further, melting of the Zn coating at the interface and subsequent alloying with the Mg sheet resulted in formation of solidified Zn-Mg alloy layer at AZ31/steel interface.

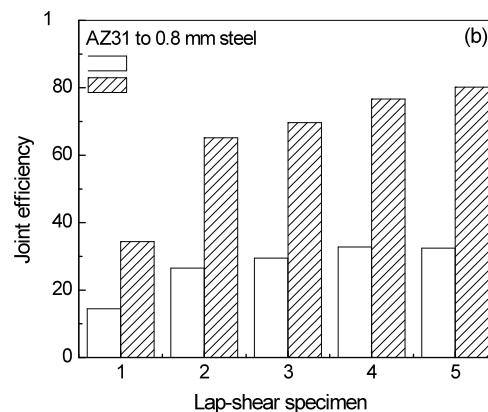


Figure 4. Joint efficiency of friction stir welds between AZ31 and mild steel.

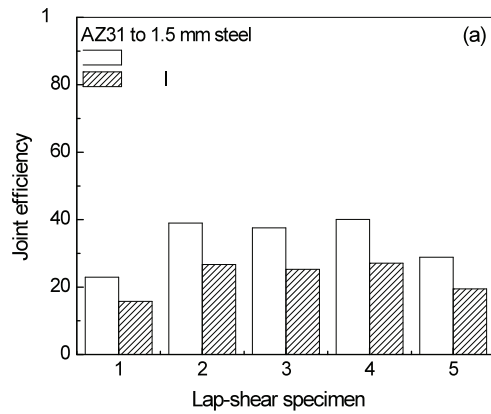


Figure 5. Joint efficiency of friction stir welds between AZ31 and HSLA.

To get a better idea about the joint interface characteristics, extensive optical microscopy was carried out. Figures 6 and 7 compare the cross-section macrographs of the two different welds studied. It is evident that in both weld conditions, the bottom steel sheets were deformed. However, the extent of the deformation of the bottom sheet is much more in the case of the 0.8-mm mild steel sheet. It should be noted that for both welds identical target plunge depths of 2.45 mm were used. However, for a 1.5-mm-thick HSLA steel sheet the steady state plunge depth was noted to be 2.38 mm, whereas, in case of a 0.8-mm steel sheet steady state plunge depth was 2.35 mm. Wider lateral deformation of the bottom steel sheet in the case of the 0.8-mm weld was related to its inherent lower strength. The distance between two hooks, region D in Figure 6, was found to be 1.89 mm for the 1.5-mm steel weld. In the case of the 0.8-mm steel sheet, Figure 7, the distance between similar features was measured at 5.17 mm.

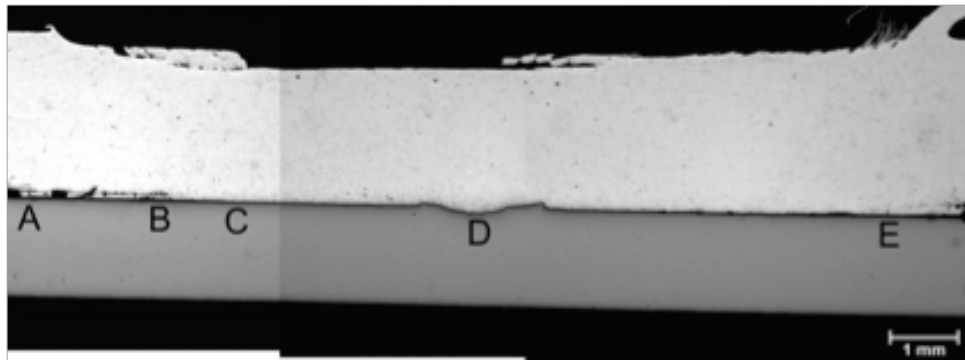


Figure 6. Cross-section macrograph of AZ31 to 1.5-mm steel weld

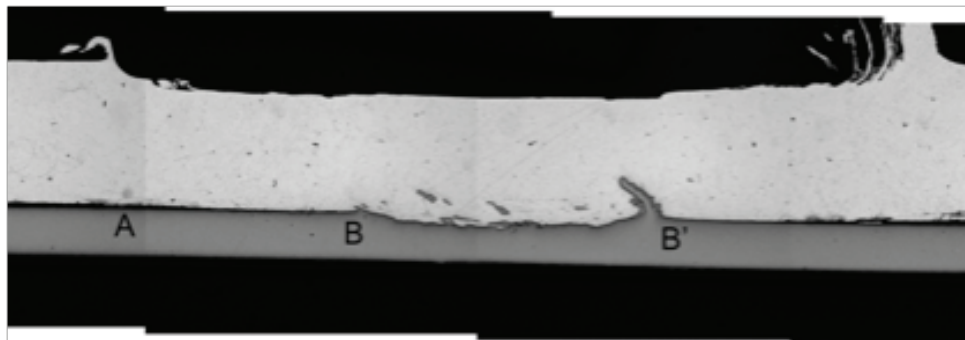


Figure 7. Cross-section macrograph of AZ31 to 0.8-mm steel weld

To better understand the microstructural characteristics at the interface, the same locations were observed via optical microscopy and were characterized with SEM. The presence of three different phases is evident in Figure 8, which is a magnified image of the location along the right

hook shown in Figure 7. Further analysis revealed this new third phase to be a Zn-Mg alloy. This more detailed SEM investigation of the new Zn-Mg phase showed the presence of hexagonal-shaped bright particles as well as lamellar and spiral structures that are shown in Figure 9. Some of the new material is entrapped between the steel and the AZ31. Otherwise, the interface is found to be devoid of any new material. Nevertheless, the presence of both the spiral and the lamellar structures indicated this new phase was a product of solidification, a formation structure well documented in literature.

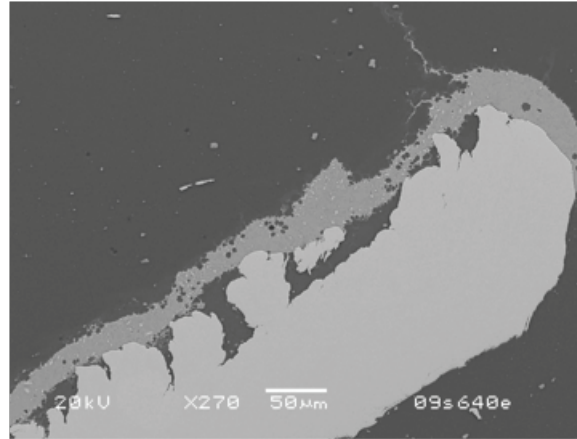


Figure 8. SEM images of AZ31 to 0.8-mm EG steel weld. (a) New Zn-Mg phase near the hook

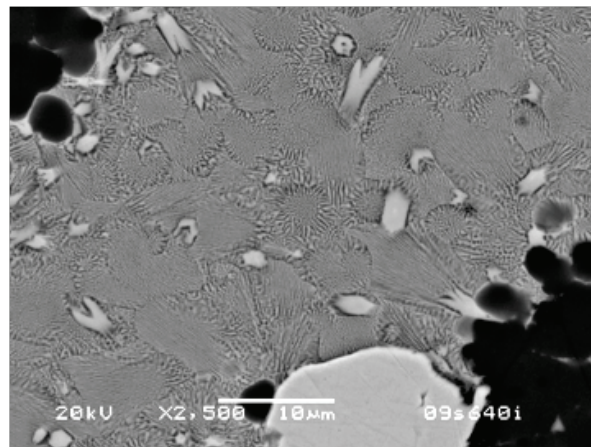


Figure 9. Solidification microstructure inside Zn-Mg phase and hexagonal particles

Ultrasonic Welding

Preliminary ultrasonic welds were made with a Sonobond CLF2500 using a pedestal welding station. The rated conditions at the welding tip on this equipment are 20-kHz frequency with 25 micrometers (mm) amplitude. The sonotrode tip was made from T1 steel, and it had a flat, rectangular face of 7 mm x 7 mm as shown in Figure 10. The line pressure to the tip clamping mechanism was adjusted to make the welds under constant nominal pressure of 39 megapascals (MPa).

The materials used for these experiments were sheets of 0.8-mm-thick hot-dip-galvanized (HDG) mild steel and 1.6-mm-thick AZ31B-H24. The steel is unetched with a zinc coating of about a 9-µm thickness. The microstructure on cross-sectioned surfaces of the AZ31B-H24 is consistent with its strain-hardened condition.

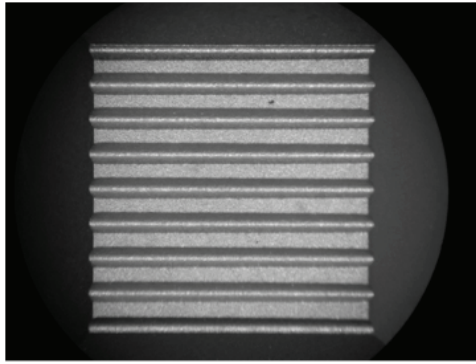


Figure 10. Photograph of the face of the 7-mm-x-7-mm sonotrode tip.

Prior to welding, the surfaces of the AZ31B sheet were buffed with non-metallic abrasive pads (Scotch-Brite™) to remove surface oxides and produce shiny surfaces. Several welds were also attempted where the Zn coating was removed from the steel surface by grinding. Both metals were cleaned with acetone followed by isopropyl alcohol to remove lubricants and surface debris.

Coupons of AZ31 nominally 30 mm wide x 100 mm long were welded to mild steel coupons of the same size to produce specimens for lap-shear testing. A 25-mm overlap was used for making lap-welded coupons with spot welds centered in the overlap regions. The specimens were not shimmed in the grips, and no guides were used to constrain specimen rotations during testing. Specimens were positioned for welding so that the primary vibration direction of the sonotrode was perpendicular to their long axis.

Spot welding was performed using a power of 1500 W at an impedance setting of 6. Welding times from 0.2-1.2 seconds (s) were evaluated, and a total of 4 specimens were made at each welding condition. Of these, three were used for tensile lap-shear testing at a cross-head speed of 10 mm/min. The fourth specimen was reserved for metallographic examinations. Selected specimens were examined by optical and scanning electron microscopy.

The results of the tensile lap-shear testing are presented in Figure 11 where the variation of failure load with welding time is plotted. There was an initial rapid rise in lap-shear failure load from ~0.5 kN to near 2.9 kN as the welding time increased from 0.2-0.4 s. After the rapid increase, failure loads continued increasing with welding times but at a much lower rate. From 0.4-1.2 s, failure loads increased to a maximum average value of 4.2 kN. Linear regression was used to calculate the line representing these data (Figure 11). At the shorter welding times, scatter in the strength was relatively high, and the dashed line representing these data was added to highlight the overall trend. Welds of the AZ31 to bare steel were unsuccessful. Weak bonding occurred in this case, but joints could be easily broken by hand.

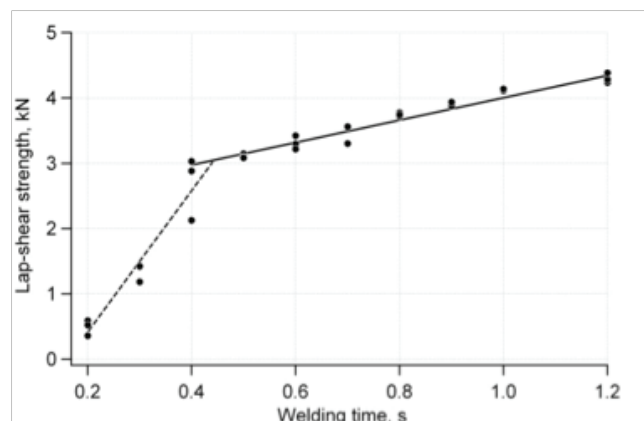


Figure 11. Variation of lap-shear strength with welding time.

The lap-shear strength results can be placed in perspective by comparison with data from resistance spot welds and FSSWs of AZ31. The pioneering work of Klain and coworkers [1] confirmed that AZ31 could be resistance spot welded and measured lap-shear strengths ranging to 5.7 kN. Lap-shear strengths increased with spot diameters and were about 4.0 kN for diameters with areas equivalent to 7 x 7 mm. More recent work by Lang and coworkers [2] measured lap-shear strengths up to 3 kN for spot welds of AZ31 with nugget diameters of about 7 mm. Pan and coworkers [3] showed that AZ31 sheet could be friction stir welded and some joints had lap-shear strengths as high as 4.75 kN. No comparable published data could be found for Mg-steel spot-welded joints made by these two processes. Nevertheless, strengths for ultrasonically-welded joints at times greater than about 0.5 s consistently exceeded 3 kN and so they are generally consistent with values found for Mg-Mg joints.

Important features of joint microstructures are highlighted in Figures 12 and 13, where unetched views of the Mg-steel interfaces are shown for welds made respectively at 0.3 s and 1.0 s. In both of these optical micrographs the AZ31 is situated at the top and the HDG steel at the bottom. Figure 12 clearly shows that two reaction layers exist at the Mg-steel interface after 0.3 s. In contrast, Figure 13 indicates that after 1.0 s the interface layers are no longer visible.

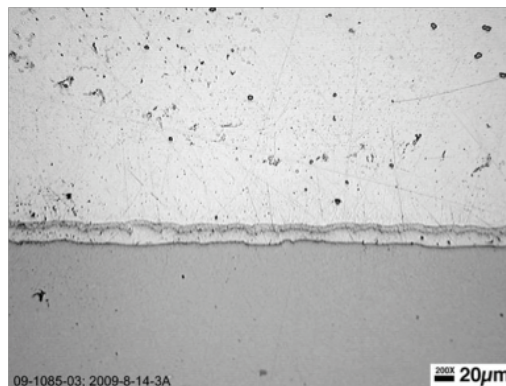


Figure 12. Optical micrographs showing cross-sectional view of AZ31 (upper sheet) welded to HDG steel (lower) in 0.3 s (shown unetched).

An SEM micrograph of the 0.3-s weld is shown as Figure 14 where the interface layers are labeled L1 and L2. The combined thickness of the layers is about 22 mm, somewhat greater than the 10-13-mm thickness of the original Zn coating. The L1 layer at the AZ31 surface was ~6 mm thick and appeared to consist of multiple phases. Its chemical composition, determined by energy dispersive spectroscopy, averaged 25.5 at% Zn with a balance of mainly Mg. This composition is in the vicinity of a Mg-Zn eutectic which occurs at 28.1 atom percent (at%) Zn and 344°C. The L2 layer in contact with the steel surface was ~16 mm thick and also appeared to be multi-phased. The overall composition of this layer averaged 66.3 at % Zn with a balance of Mg.

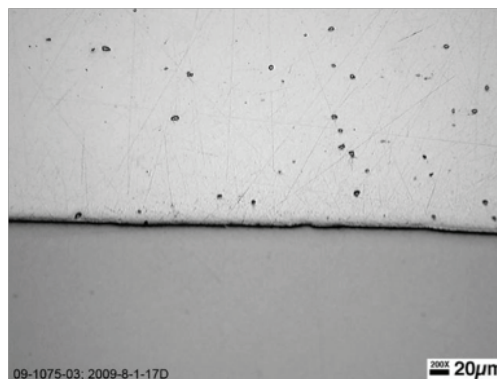


Figure 13. Optical micrographs showing cross-sectional view of AZ31 (upper sheet) welded to HDG steel (lower) in 1.0 s (shown unetched).

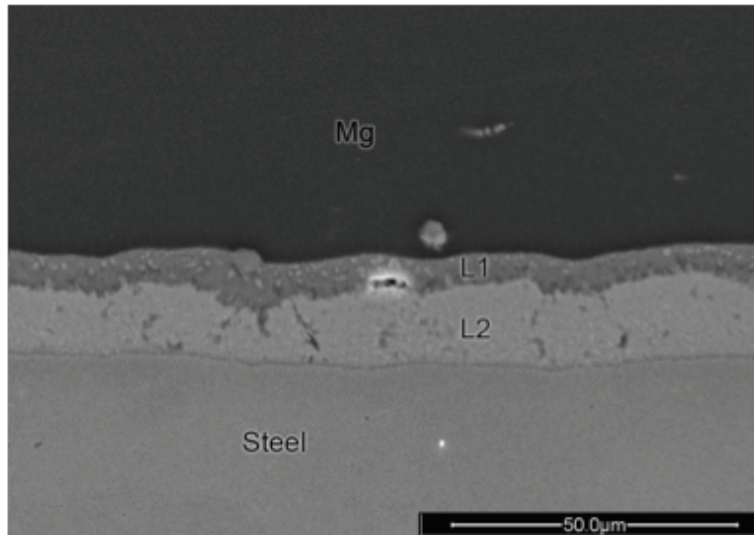


Figure 14. Secondary electron SEM micrograph showing the interface layers, L1 and L2, of the 0.3-s weld.

The observation that weak bonding was possible when the Zn was removed from the steel surface indicates that Zn is an essential element of the mechanism of bonding the AZ31 to steel by ultrasonic spot welding. With the HDG coating intact, ultrasonic spot weld strengths were comparable to those of Mg-Mg spot welds made by resistance spot welding and friction stir spot welding. Evidence for heat generation during the ultrasonic spot welding is confirmed by the microstructures of both the AZ31 sheet and the joint interface layers. The AZ31-H24 clearly experienced recrystallization and grain growth as welding time increased from 0.3-1.0 s. This could only occur if the temperature of the AZ31 was elevated beyond a critical value likely to be several 100°C. The discovery of two reaction layers between the AZ31 and steel in the 0.3 s weld confirmed that chemical reaction occurred very rapidly between the Mg and Zn. The composition of the multi-phase layer at the Mg surface, near 25 at% Zn, confirms that the temperature at the original AZ31-HDG steel surface must have reached at least 344°C. The higher Zn/Mg ratio of the layer in contact with the steel surface is consistent with mass transport of Mg toward the steel surface. The absence of the reaction layers in the 1.0-s weld suggests that the Mg-Zn layer completely liquefied and was largely squeezed from the interface by the pressure applied during welding. The conclusion that heat generated significant temperature rise at the joint interface during welding is consistent with other work [4] on bonding mechanisms in ultrasonic welding. The heat must have been generated by friction associated with the rubbing action produced by the ultrasonic welding process.

Conclusions

Project performance throughout this year allowed for all 2009 milestones to be successfully achieved. With continued support from several industrial advisors and the collaborative effort from research staff at PNNL and ORNL, increased understanding of the joining mechanisms possible between magnesium and steel was achieved. Progress during this period has ultimately allowed the joint efficiencies of solid state welds between magnesium and steel to be increased from 40% to beyond 60%, surpassing the goals set for FY09 milestones. Current results have significant implications to the end user, as joint strengths in excess of 60% may be considered for structural applications between these two dissimilar materials. Additionally, this is a midpoint milestone demonstrating that the DOE investment in this technology development is providing the understanding necessary to achieve the ultimate goal of joint strengths in excess of 75%. The successful progress made to date in both FSW and USW is crucial to expanding the technologies

needed for future implementation of lightweight dissimilar structures. The understanding of the mechanisms and relationships of process parameters on joining magnesium to steel developed in this program are providing the fundamental baseline needed to critically evaluate the potential for expanding the usage of magnesium in any future automobile.

References

P. Klain, D. L. Knight, and J. P. Thorne, "Spot Welding of Magnesium with Three-Phase Low Frequency Equipment," *Welding Journal*, vol 32, (1953) pp. 7-18

B. Lang, D. Q. Sun, G. Z. Li, and X. F. Qin, "Effects of welding parameters on microstructure and mechanical properties of resistance spot welded magnesium alloy joints," *Science and Technology of Welding and Joining*, vol. 13, (2008) pp. 698-704

T.-Y. Pan, M. L. Santella, P. K. Mallick, A. Frederick, and W. J. Schwartz, "A Feasibility Study on Spot Friction Welding of Magnesium Alloy AZ31," in IMA 2006 World Mg Conf., Beijing. Proceedings of the 63rd Annual World Magnesium Conference in Beijing (2006) Intl. Magnesium Assoc., Wauconda, IL USA

J. B. Jones, N. Maropis, J. G. Thomas, and D. Bancroft, "Phenomenological Considerations in Ultrasonic Welding," *Welding Journal*, vol. 40, (1961) pp. 289-s-305-s

E. Friction Bit Joining—An Innovation in Dissimilar Metal Joining

Principal Investigator: Zhili Feng
Oak Ridge National Laboratory
1 Bethel Valley Road; Oak Ridge, TN 37831
(865) 576-3797; e-mail: fengz@ornl.gov

Co-Principal Investigator: Michael P. Miles
Brigham Young University
265 CTB; Provo, UT 84602
(801) 422-1858; e-mail: mmiles@byu.edu

Technology Area Development Manager: William Joost
(202) 287-6020; e-mail: william.joost@ee.doe.gov

Field Technical Monitor: C. David Warren
(865) 574-9693; e-mail: warrencd@ornl.gov

Contractor: Oak Ridge National Laboratory (ORNL)
Contract No.: DE-AC05-00OR2272

Objective

- Develop the technical basis and demonstrate the viability of a newly invented solid-state joining process—friction bit joining (FBJ)—for joining dissimilar metals such as aluminum (Al) or magnesium (Mg) alloys to advanced high-strength steels (AHSSs) for use in autobody structures to achieve a balance in cost savings, lightweighting, structural durability, and impact performance.

Approach

Phase I (Concept Feasibility):

- Perform Design of Experiment (DoE) to determine the key process variables and factors that influence the bonding process and the joint strength.
- Characterize bonding interface to develop basic understanding of the bonding mechanisms between dissimilar metals in FBJ.
- Develop the baseline welding conditions for different material and gauge combinations.
- Determine the feasibility of FBJ with adhesive (weld bond).
- Perform initial figure of merit (FOM) analysis to compare FBJ with other dissimilar metal joining processes.

Phase II (Technical Feasibility):

- Joining bit design and optimization for joint strength (static, fatigue and impact).
- Process and equipment improvement/optimization.
- Corrosion prevention/mitigation.
- Prototype body component fabrication and evaluation by OEMs.
- Business case study including cost-benefit analysis and technology insertion opportunities.

Accomplishments

- Met or exceeded the milestones and target metrics set forth for Phase I concept feasibility study:
- Demonstrated the feasibility of FBJ of dissimilar metals (Mg to steel and Al to steel) with excellent joint strength far superior than alternative processes for dissimilar metal joining (FSSW, UW, SPR).
- Achieved metallurgical interfacial bonding between different metals.
- Achieved reasonably fast process time (less than 2s) and relatively low process load (comparable to RSW and much lower than SPR) that consistently produced excellent joint strength.
- Demonstrated feasibility of combining FBJ and adhesive bonding.
- Completed initial FOM analysis and business case study for the technical and economic viability of the FBJ.

Future Direction

- Continue bond interface characterization and bonding mechanisms investigation.
- Joining bit design and optimization for joint strength (static, fatigue and impact) and cost.
- Process and equipment improvement/optimization, including mechanized joining bit feeding system for high-speed, high-volume production.
- Corrosion prevention/mitigation.
- Prototype body component fabrication and evaluation by OEMs.
- Business case study including cost-benefit analysis and technology insertion opportunities.
- Explore and develop technology transfer and commercialization partnership.

Introduction

The automotive industry and the Department of Energy Vehicle Technologies Program are proactively pursuing increased use of lightweight materials such as Mg alloys and Al alloys in auto-body structures for improved vehicle fuel efficiency. Next generation vehicles will require optimum use of a variety of highly engineered materials, ranging from AHSSs to lightweight materials such as Al and Mg alloys to composites and others, to achieve a balance in cost,

lightweighting, durability, and crashworthiness. Use of vastly different lightweight material combinations in auto-body structures presents a number of technical challenges in body-in-white assembly. One of them is joining dissimilar materials to form integrated structural components to meet design and performance requirements [1,2].

Dissimilar metal joining—joining of vastly different materials such as Mg and steel, Mg and Al, and Al and steel—is generally considered to be out of the “comfort zone” of the existing joining and attachment technologies used in high-volume mass production. Conventional welding processes that involves melting (such as gas metal arc welding, laser welding, and resistance spot welding), are not suitable for welding dissimilar materials, because of the metallurgical incompatibility of these materials during melting and solidification. Dissimilar metals can be mechanically bolted or fastened together, but it is undesirable due to the low productivity and added weight to the structure. Self-piercing riveting (SPR), a relatively fast and highly mechanized process, has been used in the past to join Al alloys to steels. However, SPR is difficult to apply to AHSSs typically having tensile strength above 900MPa, because of the inadequate strength of rivet materials and the high load required to pierce through high-strength steels. Application of SPR for Mg alloys has additional difficulties associated with the low ductility of Mg alloys at the ambient temperature. Adhesive bonding has its own cost and performance penalties.

To address the critical technology barrier of dissimilar metal joining, the U.S. DOE’s Lightweighting Materials Program supported an initiative aimed at developing technologies suitable for joining dissimilar metals for auto body structural applications. Solid-state joining processes including friction stir welding, ultrasonic joining, and a newly invented process - friction bit joining (the focus of this project) are among the processes under development.

This project aims at investigating and developing a new solid-state joining process particularly suitable for dissimilar metals. This newly invented process – friction bit joining (FBJ) – combines the process advantages and overcomes the fundamental shortcomings of the friction stir spot welding process and the mechanical SPR process.

A two-phase, gated approach is adopted in this project. Phase I was a Concept Feasibility study with the following two primary objectives: (i) determining major factors influencing the joint strength and the underlying microstructural characteristics of the bonding interface, (ii) determining whether sufficiently strong weld can be produced for Al-to-steel and Mg-to-steel in reference to the industry specifications and other available information of alternative processes and methods. If warranted, more comprehensive R&D will be carried out in Phase II (Technical Feasibility) of the project that includes process optimization, prototype system development, corrosion prevention/mitigation, business case study for technology insertion, and eventual field demonstration of the FBJ technology. Phase II will also include identifying potential commercial partners and eventual partnership with technology transfer and commercialization candidates.

The Phase I effort was co-sponsored by U.S. DOE’s Lightweight Materials Program and National Science Foundation’s Materials Processing and Manufacturing Technology Program and jointly carried out at ORNL and Brigham Young University.

The Phase I study was been completed successfully in FY2009. This report presents the key developments in Phase I, highlighting the accomplishment toward the milestones and deliverables set forth for the Phase I study.

Process Principle of FBJ

FBJ creates a metallurgically bonded spot joint in two or more sheets of the same metal or dissimilar metals by utilizing a consumable joining bit. The essence of FBJ is illustrated in [Figure 1](#), in comparison with the more common FSSW process. The FBJ process starts with an initial phase where the top layer (or layers in multi-stack configuration) is penetrated by the rotating

joining bit driven by the plunging axial load. The process then transitions to the frictional joining phase in which the spindle speed increases to several thousand RPM so that the rotating bit and surrounding sheet materials are frictionally heated to a high temperature to facilitate material flow and bonding. At the end of the operation, a metallurgical bond is formed between the joining bit and the sheet materials as a result of atoms of different metals diffusing across the interface under high temperature and high pressure, in a manner very similar to friction stir welding. FBJ is also similar to the friction stir spot welding (FSSW) process. FBJ, however, uses a consumable joining bit that forms an integral part of the weld. As demonstrated in this study, the use of the consumable joining bit in FBJ results in a much larger bonding interface area and considerably improves the joint strength over these made by the FSSW process.

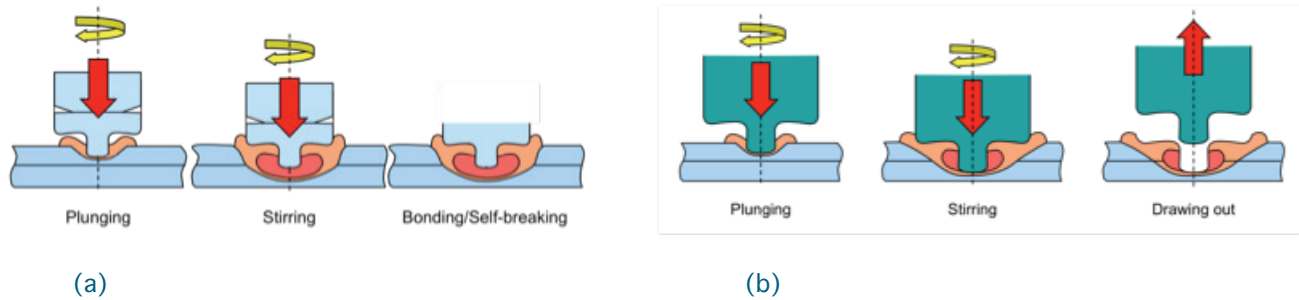


Figure 1. Schematic representation of (a) FBJ process and (b) FSSW process.

Prototype FBJ machine

A prototype machine, shown in Figure 2, was designed and built for FBJ. The electric motor driven spindle head design had a special control mechanism that can stop the rotation in about 25 microseconds – a feature necessary to produce joints with consistent quality and repeatability. This first-generation research machine also had a Cframe similar to that commonly used in robotic RSW machines. As shown in the figure, the C-frame in this first prototype machine was quite bulky because it was designed for an axial load anticipated over 30kN. However, surprisingly low axial loads were obtained in the welding trials conducted in Phase I. They ranged from 8 kN to 12 kN, only marginally higher than the forces used in RSW of AHSS. Therefore, the C-frame in future FBJ machine designs could be reduced to the size of C-frames on RSW machines.



Figure 2. Prototype FBJ machine with a Cframe.

A second-generation research type FBJ machine is being designed and under construction. This new machine incorporates many improvements and new features based on the lessons learnt in Phase I of the project. The new machine will be available in March 2010.

Joining Bit Design

The early joining bit design investigated in Phase I of the project had a shank that was inserted into the joining bit holder of the prototype FBJ machine. This joining bit design incorporated a unique self-break-off feature – the shank is automatically sheared off at the end of the operation, leaving a relatively smooth joint surface above the bit flange, as shown in [Figure 3](#). The unique self-break-off feature makes it possible to automate the process in production environment and eliminate the need for the after-welding cutting operation.



Figure 3. Appearance of FBJ between DP 980 AHSS and AA 5754 aluminum.

A shank-free joining bit design was developed and successfully demonstrated at the second half of the Phase I study. The shank-free design further shortened the joining process time by 0.4 to 0.5 second that was required for the self-breaking-off action. A total welding cycle to 1.6 second has been achieved in Phase I. The shank-free design also solved the issue of shank recycling, as well as simplified the control system of the FBJ machine.

Process Development

Experiments were carried out on two material combinations: 1.4 mm thick uncoated dual phase (DP) 980 steel welded to 1.8 mm thick Al alloy 5754 (AA 5754-O), and 1.4 mm thick uncoated DP 980 welded to 1.8 mm thick Mg alloy AZ91. All welding trials were on as-received surface conditions.

In Phase I, the strength of the dissimilar metal joints was primarily evaluated using the lap-shear tensile test. The lap-shear testing specimen had nominal dimensions of 25.4mm wide and 101.2 mm long, with a 25.4mm overlap in the joint area. The spot weld was produced in the center of the overlapping area. Spacers were used during the lap-shear tensile test to ensure the specimen was centered along the tensile axis.

Joining DP980 to AA5754

A design of experiment (DoE) study was carried out to develop the baseline understanding of the key process variables to the joint strength and quality. The following process variables were evaluated systematically in the DoE study:

Joining bit:

- Three alloy steels (4140, 4340, D2) heat-treated to hardness levels from 15 to 55Rc
- Bit length
- Shape design (flat or fluted)

Process parameters:

- Welding time
- Cooling time
- Plunge Rate
- RPM

Figure 4 provides an example of the DoE testing results with 4340 steel joining bit. In this particular case, the original joining bit design with the shank was used. A “cooling cycle” was required to “self-break-off” the shank part from the welded part at the end of the welding. It was found that combination of longer welding time (1.5 sec), short cooling time (0.5 sec) and short joining bit length increases the strength of the joint.

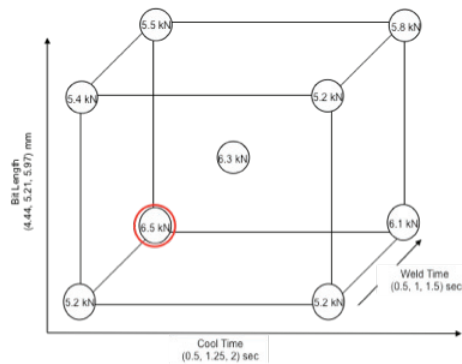


Figure 4. Averaged lap-shear joint strength from DoE study of joining DP980 to AA5754 with 4340 “flat” joining bit heat treated to 15Rc. 6.2mm bit diameter.

Overall, the FBJ process can be quite repeatable. As an example, Table 1 shows the joint strengths of DP980-AA5754 joints made with two different bit designs (flat bit and fluted bit). The short process cycle time (1.5s welding + 0.5s self-breaking) resulted in great lap shear strength for both “flat” and “fluted” bit designs. Both joining bit designs achieved the minimum joint strength of 5900 lbs under 1.5 sec of welding time. Whereas the flat bit design showed more consistency, the fluted bit design reached maximum strength of 7350 lbs which effectively caused a wider range of the joint strength. The highest lap-shear strength achieved in Phase I was 8120N (1825lbf).

Table 1. Repeatability of joint strength of DP980-AA5754 joints. Welding time: 1.5 sec. Joint bit material: 4140 steel @ 30Rc. 6.2mm bit diameter.

	flat bit design	fluted bit design
Sample #	Lap Shear Strength (N)	Lap Shear Strength (N)
1	6417	5758
2	6715	7351
3	6061	6412
4	5834	5905
5	5959	7111
Ave	6197	6508
Range	881	1593

The dominant failure mode for the lap shear specimens produced with 1.5 sec welding cycle time was the fracture of the base metal aluminum sheet. As seen in [Figure 5](#), the aluminum sheet failed around the joining bit whereas the joining bit itself remained to be bonded to the DP 980 sheet. 80% of specimens failed in this manner, while the other 20% failed by fracture of the joining bit (either button pullout or interfacial fracture).



Figure 5. Failure of AA5753 base metal sheet during lap-shear tensile test of a DP980/AA5754 FBJ specimen.

[Figure 6](#) further illustrates in the cross-sectional view the failure location of a DP980/AA5754 joint corresponding to that in [Figure 5](#). The failure location is clearly away from the bonding interface. Therefore, our Phase I work demonstrated that the bonding interface created by the FBJ process is so strong that the failure of a joint is controlled by the strength of the base metal. In other words, the bonding interface in FBJ is no longer the weakest region of a dissimilar metal spot weld, as in the case of FSSW and UW [3,4].

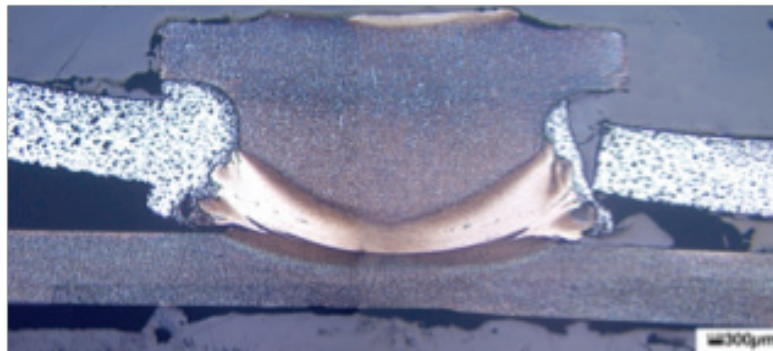


Figure 6. Cross-section of a broken friction bit joint between DP980 and AA5754. Lap-shear loading condition. Failure load = 8210N.

Joining DP980 to AZ31

The Phase I study on dissimilar metal joining between steel and Mg alloy was also quite successful. [Table 2](#) shows the lap-shear tensile strength of DP980/AZ31 joints made by FBJ with a welding time of 1.5s and self-breaking time of 0.5s. The average joint strength of 10 repeated specimens was 5232 N, much higher than the recent results from the parallel UW study. The joint strength was very consistent, with a very tight range of 325N.

Table 2. Lap-shear strength of 10 DP980/AZ31 friction bit joints made using the same process parameters. Fluted 4140 steel bit. 6.2mm bit diameter.

Sample #	Lap Shear Strength (N)
1	5340
2	5140
3	4975
4	5255
5	5260
6	5255
7	5402
8	5162
9	5104
10	5429
Ave	5232
Range	325

Over 80% of DP980/AZ31 FBJ failed in the AZ31 base metal sheet during lap-shear tensile test as shown in Figure 7. Again, the excellent bonding was demonstrated in Phase I for FBJ of steel to Mg alloy.

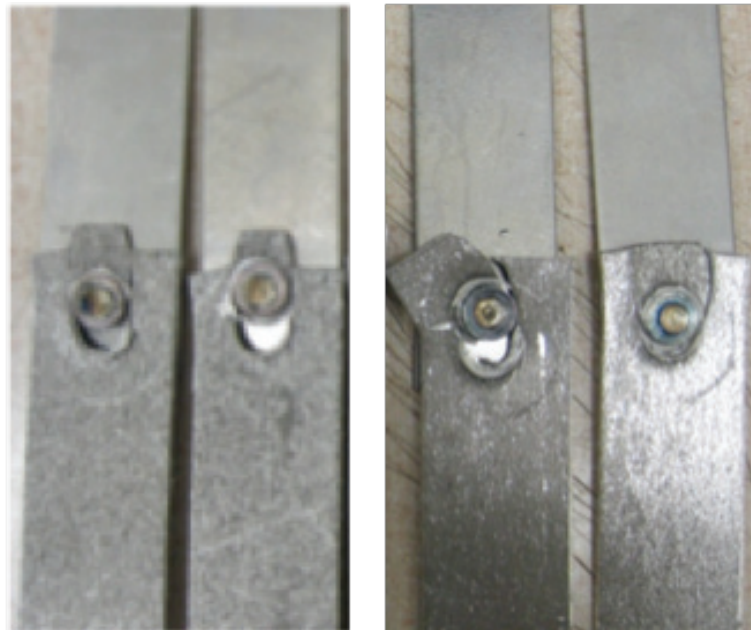


Figure 7. Predominate failure mode of DP980/AZ31 FBJ during lap-shear tensile test: shearing of AZ31 base metal.

Microstructural Characterization of Bonding Interfaces

The bonding interfaces of FBJ were characterized in Phase I using various analytical microscopes to provide a basic understanding of the bonding mechanisms. Figure 8 shows an example of FBJ spot welds made between AA 5754 and DP 980. Figure 9 presents the details of the bonding interface between the steel and the Al sheet at four different locations (see labels in Figure 8). The metallurgical bonding is clearly achieved between the steel and Al alloy. This is supported by the EDS and WDS micro-chemistry analysis of the interface, as shown in Figure 10 and Figure 11 respectively. Furthermore, the transition of Fe and Al at the interface is rather gradual. The formation of intermetallic phases between Fe and Al is not evident.

Metallurgical bonding was also achieved between DP 980 steel and Mg alloy AZ91, as shown in the WDS analysis of the interface in Figure 12.

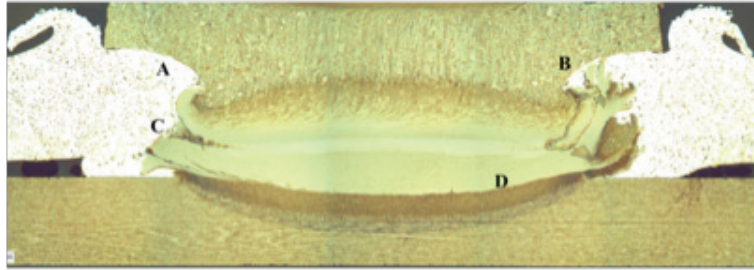


Figure 8. Cross section of FBJ composed of AA 5754 (top sheet), DP 980 (bottom sheet), and 4140 steel joining bit (center).

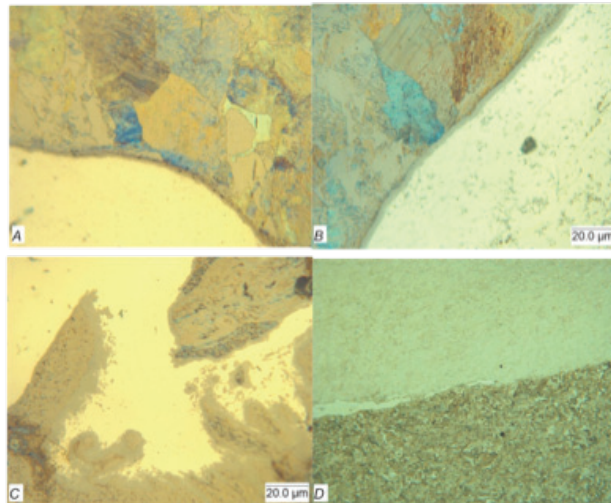


Figure 9. Bonding interface between AA 5754 and DP 980. Metallurgical bonding is evident.

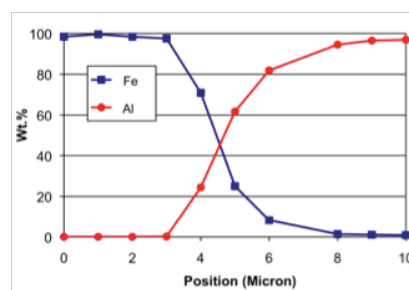
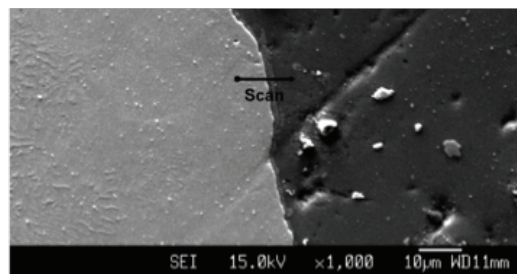


Figure 10. EDS Micro-chemical analysis at Al-steel interface in FBJ joint.

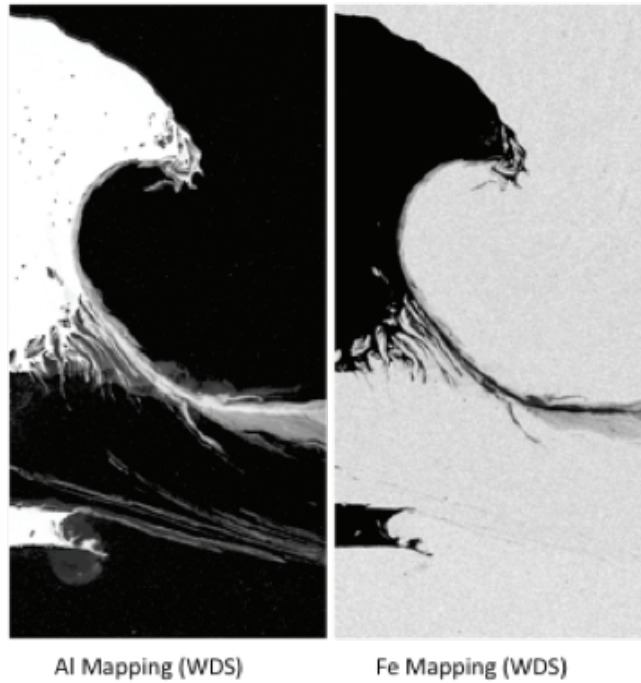


Figure 11. WDS mapping of Al and Fe in a DP980/AA5754 friction bit joint.

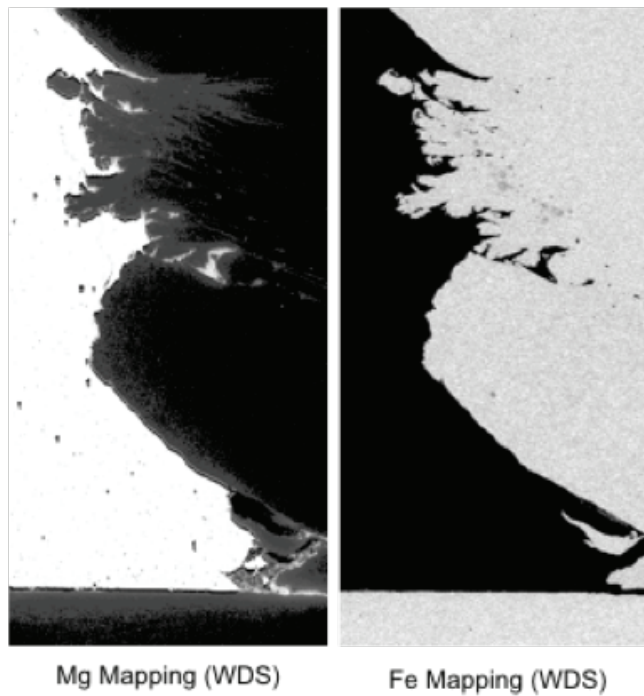


Figure 12. WDS mapping of Mg and Fe in a DP980/AZ31B friction bit joint.

Figure 8 also reveals another important feature of the FBJ. The top Al sheet is joined to the steel joining bit through a combination of microscopic metallurgical bonding and mechanical interlocking associated with the extensive deformation/material flow of the joining bit. Further, the extensive deformation of the joining bit increases the effective bonding area between the dissimilar metals (steel and Al). It is reasoned that it is the combined metallurgical bonding and mechanical interlocking that contributes the superior bonding strength of the steel to Al interface, resulting in failure in the base metal region of the Al sheet as shown in Figure 6 and a higher joint strength than the comparative SRP which presented in the next section.

Comparison with SPR

A comparison between FBJ and SPR was done on a combination of 1.6 mm DP 590 and 1.8 mm AA 5754-O. This combination was used because SPR of very high strength steels is difficult, and therefore DP 980 was not used [5]. For both types of joints, the AA 5754-O was on top while the DP 590 was on the bottom. For SPR a 6mm diameter 60752 Emhart Tucker rivet was used for joining, while for FBJ a 6.5 mm 4140 steel bit was employed. The SPR was made at General Motor's Technical Center using its SPR equipment and procedure. A cross section was done to ensure that the riveted joints were reasonably sound, as seen in Figure 13.

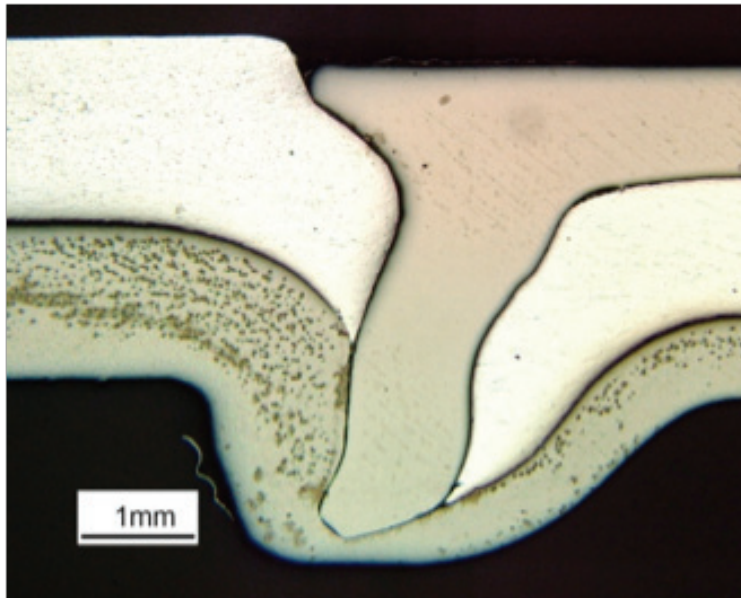


Figure 13. Cross-section of SPR joint composed of AA5754 (top sheet) and DP590 (bottom sheet).

For FBJ, lap shear strength, as an average of 5 specimens, was 6.4 kN, with a range of .37 kN. The average lap shear strength of SPR of 5 samples was 5.3kN with a range of 0.4kN. The SPR results were also in line with data from the literature for bonding of a dissimilar Al/steel combination [6]. The joint strength of FBJ is about 20% higher than that of the SPR for the same combination of materials.

Preliminary trials of SPR between DP590 and Mg AZ31B were unsuccessful, due to premature cracking and shattering of AZ31B during joining.

Finally, FBJ and SPR are compared on “unit bonding area” basis. Sun et al. [6] reported SPR experiments performed on combinations of high-strength, low-alloy (HSLA) 350 steel and AA 5754. Although the steels used in the two studies were different (DP 980 vs. HSLA350), the weaker material (AA5754) was the same in both studies and provides the basis for comparison. To effectively compare FBJ and SPR, the bond areas must be known because bond area affects the strength of the joint. The bond area for the FBJ joints was determined by optical measurement of the fracture surface across two diameters of the weld, 90° apart. SPR results can be found in reference [6]. The bond area for the FBJ joints was 28 mm² and for the SPR joints 47 mm². Lap shear failure loads were 6.4 kN for FBJ and about 5.2 kN for SPR. Based on these results, the FBJ joint supports a much greater load per unit bond area than the SPR joint by a factor of 2.

Preliminary Weld Bonding Trials

Phase I also included a preliminary study to evaluate the feasibility of combining FBJ with adhesive bonding (weld bonding). Weld bond, typically combining RSW with adhesive bonding, is an effective joining method to improve the crashworthiness and durability of body structures. In the case of FBJ, the use of adhesives could have additional benefit of sealing the joint region to mitigate the galvanic corrosion – a common concerns of dissimilar metal joining especially Mg to steels.

The adhesive used in Phase I was a commercially available type supplied by Ford Motor Company. The same DP980/AA5754 material combination was used, with a welding cycle of 1.6 seconds. The adhesive was applied in the joint region following the procedure commonly used in the industry. FBJ was made before the applied adhesive was cured, which is typical in weld bonding. The uncured adhesive also allows for assessment of effect of the heat from FBJ on the adhesive.

Table 3 shows the lap-shear tensile test results of 5 replicate samples made with 4140 “fluted” joint bit design with a welding time of 1.6 second. The joint strength was highly repeatable and averaged at 6425N. This suggests that the non-cured adhesive had no detrimental effect on the joint strength.

Table 3. Lap-shear testing results of FBJ with adhesives.

Sample #	Lap Shear Strength (N)
1	6550
2	6328
3	6266
4	6350
5	6631
Ave	6425
Range	365

Figure 14 shows the appearance of adhesives after the friction bit joint was tensile tested. It appeared that the effect of heat from FBJ on adhesives was very localized. Therefore, it is expected that the FBJ will have minimal impact on the strength of the adhesive after it is fully cured. Furthermore, the fully cured adhesives would be used as a sealer to mitigate the galvanic corrosion concerns of dissimilar metal joint. More study on the adhesives as way for corrosion prevention are planned in Phase II.



Figure 14. Close view of adhesive after tensile test of FBJ. Initial Figure of Merit Comparison and Analysis

Initial figure-of-merit (FOM) analysis was performed in Phase I to compare different alternative processes for dissimilar metal joining. Specifically, FBJ was compared with SPR (a process relatively mature), and FSSW and UW (two new processes under development). The FOM analysis results are summarized in Table 4.

Table 4. Figure of Merit comparison of different dissimilar metal joining processes

	FBJ	SPR	FSSW	Ultrasonic
Material Combination				
Steel to Al	yes	yes	coated steel	coated steel
Steel to Mg	yes	difficult	TBD	coated steel
Steel Grade	All AHSS	up to DP780	All AHSS	All AHSS
Stacks	2T, 3T	2T, 3T	2T	2T
Surface Requirement	no restriction	no restriction	Zn coating	Zn coating, some cleaning
Bonding Mechanism	Metallurgical + Mechanical	Mechanical	Brazing or Metallurgical	Brazing, or metallurgical
Lap shear strength (N)				
Steel to Al	6300 - 8100	5000 - 5500	2500 - 3500	~3000
Steel to Mg	~5400	cracking	N/A	4200
Z load (N)	~ 9000	20,000 or higher	TBD	~ 2000
Process Time (sec)	1.5 - 2	< 1	<4	1.2 - 2
Weld bonding	Feasible	yes	Difficult	TBD
Consumable Bit	Yes	Yes		
Cost	Comparable to SPR	low		
Nonconsumerable Tool			Yes	Yes
Cost			High	High
Machine cost	comparable	comparable	comparable	Potentially high
Machine automation	Feasible	Yes	demonstrated	Feasible

Although additional analysis would be needed to quantify certain aspects (such as cost of tool/joining bit, and machine cost), FBJ compared favorably among the four processes. FBJ is advantageous in joint strength, suitability for different material and surface combinations, and weld bonding. The welding time is comparable to others. However, similar to SPR, FBJ uses a consumable joining bit which requires an automated bit feeding mechanism.

It is important to note that all these joining processes listed above are still different stages of developed for dissimilar metal joining. The FOM of each processes will continue to evolve, and will be further evaluated as these joining technologies progress.

Future Directions

- Continue bond interface characterization and bonding mechanisms investigation.
- Joining bit design and optimization for joint strength (static, fatigue and impact) and cost.
- Process and equipment improvement/optimization, including mechanized joining bit feeding system for high-speed, high-volume production.
- Corrosion prevention/mitigation.

- Prototype body component fabrication and evaluation by OEMs.
- Business case study including cost-benefit analysis and technology insertion opportunities.
- Explore and develop technology transfer and commercialization partnership.

Acknowledgements

We would like to acknowledge the contributions of the following individuals and organizations.

Dr. L. Lev of GM for comparative studies on SPR.

Industry Advisory Committee:

Chrysler: J.E. Beckham, D.J. Zhou

Ford: E. Hetrick, W. Charron

GM: J. Quinn, B. Carlson, D. Hutchinson

USAMP Metals Joining Team

USAMP Multiple Materials Vehicle Team

Auto/Steel Partnership Joining Technologies Team

USAMP Manufacturing Team

Presentations/Publications/Patents

1. M. Miles et al., "Friction Bit Joining of Dissimilar Material Combinations of High Strength Steel DP 980 and Al Alloy AA 5754," SEA 2009 World Congress, Detroit, Michigan, Paper No 09M-0232.
2. M. Miles and Z. Feng, "Spot Joining of Dissimilar Combinations of Steel and Light Metals Using a New Consumable Bit Technology," (Invited) Joining Dissimilar Metals Conference II, American Welding Society, March 3–4, 2009, Orlando, Florida.
3. M. Miles, Z. Feng, K. Kohkoene and R. Steel, "Spot Welding of Light Metals and Ultra High Strength Steel by Friction Bit Joining," Int. Auto Body Congress (IABC) 2009, Nov 4-5. Troy, MI
4. M. Miles, Z. Feng, K. Kohkonen, B. Weickum, R. Steel, L. Lev "Spot joining of AA 5754 and high strength steel sheets by consumable bit", Science and Technology of Welding and Joining, accepted for publication.

References

1. J. F. Quinn, "Joining Challenges in the Automotive Industry," ORNL Materials Joining Advisory Committee Meeting, November 2, 2007, Oak Ridge National Laboratory, Oak Ridge, Tennessee
2. HYBRIDMAT 2: Strategies in the Joining of Hybrid Materials in Automotive Structures—a Mission to France and Germany, May 2004. Global Watch Mission Report (UK Department of Trade and Industry Global Watch Service, September 2004).

3. T. Gendo, K. Nishiguchi, M. Asakawa, and S. Tanioka, Spot Friction Welding of Aluminum to Steel, SAE 2007 World Congress, paper No. 2007-01-1703, Detroit, MI, 2007.
4. C.-Y. Lee, D.-H. Choi, Y.-M. Yeon, and S.-B. Jung, Dissimilar friction stir spot welding of low carbon steel and Al-Mg alloy by formation of IMCs, Science and Technology of Welding and Joining, 14 (3), 2009, pp. 216-220.
5. Y. Abe, T. Kato, and K. Mori, Joinability of aluminium alloy and mild steel sheets by self piercing rivet, Journal of Materials Processing Technology, 177, 2006, pp. 417-421.
6. X. Sun and M. A. Khaleel, "Strength estimation of self-piercing rivets using lower bound limit load analysis," Science and Technology of Welding and Joining, 10(5), pp. 624-625 (2005).

F. Weld Element and Joining Process Technology Development

Principal Investigator: Douglas J. Bammann
Professor, Mechanical Engineering
Mississippi State University
210 Carpenter Bldg.
Mississippi State, MS 39762
(662) 325-3260; e-mail: djb215@me.msstate.edu

Co-Principal Investigator: Sergio Felicelli
Associate Professor
Mechanical Engineering
Carpenter Engineering Bldg, Rm 210
Mississippi State, MS 39762
(662)325-1201; e-mail: felicelli@me.msstate.edu

Co-Principal Investigator: Liang Wang
Assistant Research Professor
Center for Advanced Vehicular Systems, CAVS 2182-B
Mississippi State University, P.O. Box 5405
Mississippi State, MS 39762-5405
(662) 325-9235; e-mail: liangw@cavs.msstate.edu

Co-Principal Investigator: Ted Belyteschko
McCormick Professor of Computational Mechanics
Walter P. Murphy Professor of Computational Mechanics
Departments of Civil and Mechanical Engineering
Robert R. McCormick School of Engineering and Applied Science
Northwestern University
2145 Sheridan Road
Evanston, Illinois 60208-3111
(847) 491-7270; e-mail: tedbelytschko@northwestern.edu

Co-Principal Investigator: Wing Kam Liu
Walter P. Murphy Professor of Mechanical Engineering
Director of the NSF Summer Institut Postdoctoral Associate e on Nano Mechanics and Materials
Robert R. McCormick School of Engineering and Applied Science
Northwestern University
Department of Mechanical Engineering
2145 Sheridan Road
Evanston, Illinois 60208-3111
(847) 491-7094; e-mail: w-liu@northwestern.edu

Technology Area Development Manager: William Joost
(202) 287-6020; e-mail: william.joost@ee.doe.gov

Contractor: Colorado School of Mines
Contract No.: National Science Foundation Award CMMI -0729114

Objective

Develop the next generation of weld element technology and joining process technology (i.e., spot welding) and assess the applicability of new technology for impact simulations and process optimization using lightweight alloys.

Approach

Currently, weld element performance and failure are based on a simple beam model in which the weld is modeled as a single element between two welded sheets, and failure is postulated to occur when the tension or a moment exceed a certain specified threshold. This type of model does not reflect the thermo-mechanical details of the welding process, and consequently is unable to address variations in strength due to differences in weld process parameters and the metallurgy of the materials being joined.

To develop the next generation of weld analysis technology in which details of the welding process and the metallurgy of the parent material are reflected in the behavior of the weld element, the physics of the resistance welding process must be modeled in detail. The nature of the solidification process within the weld will be studied. The computed thermal history induced during the welding process will be used to predict microstructural evolution within the weld and adjacent material, thereby allowing prediction of the large mechanical property gradients associated with the weld. The evolution of damage in the weld under subsequent high strain rate loading will be studied with strain rate dependent constitutive models.

The development of resistance spot welding process has remained largely empirical because the process is extremely complex due to friction-induced deformation and heat generation. We plan to assess the feasibility of developing a weld element technology and a 3-D process model which will enable a better design of the spot welding process.

Accomplishments

- Microstructure, nugget size, hardness, texture, and grain size were examined for AISI 1018 spot weld samples
- Using the commercial welding software SYSWELD, an electro-thermo-mechanical finite element model was developed, which considers also the effect of metallurgical phase transformations. The model was employed to predict the temperature history, nugget size growth, and the residual stress field during different stages of resistance spot welding. The effects of welding parameters such as current, pressure, and weld cycles on residual stress distribution were investigated.
- To validate the predicted stresses neutron diffraction residual stress mapping was used to characterize the through-thickness stresses and surface stresses in a spot welded steel joint. The origin of the residual stress distribution is discussed based on the thermal histories of the samples, and the calculated stresses are compared with measurements obtained by neutron diffraction mapping.

Introduction

Resistance Spot Welding (RSW) is a common joining process used in automotive manufacturing with thousands of spot welds in a single vehicle. The process involves rapid heating and cooling rates, and yields a complicated interaction of thermal, electrical, metallurgical, and mechanical phenomena, which results in non-uniform strain and stress distributions. The residual stress has

a significant effect on the properties of the welded joint, including the brittle fracture, crack propagation, fatigue life reduction, stress corrosion cracking and so on [1, 2]. Therefore it is extremely important to understand the behaviors of strain and stress during the RSW process.

In the last two decades, simulations of the RSW processes have been carried out and developed by numerous researchers. In early 1990's, most of modeling research were carried out to study the nugget size growth, temperature and voltage distribution using coupled electrical-thermal-mechanical model [3-8]. For example, Gould (1987) studied nugget development during the RSW process and compared the predicted nugget size with the measured data [5]. Cho and Cho (1989) developed a finite difference model to predict the temperature and voltage distributions during the RSW process [7].

Residual stress was not taken into account in the aforementioned studies. Schroeder and Macherauch (1983) developed a numerical model to predict the residual stress, but only for one welding condition [9]. Anastassiou et al. (1990) analyzed residual stress distribution in spot welded steel sheets by X-ray diffraction, and investigated the effect of stresses on spot weld fatigue behavior. They found that the residual stress distribution contains high tensile stresses (400 MPa) at the center of the weld [10]. Khan et al. (2000) developed a thermal-electrical-mechanical model taking into account phase change and convective transport in the molten pool. The model predicted the nugget development during the RSW process of Al alloy, but the residual stress was not predicted [11]. Sun et al. (2000) also developed a model to simulate the RSW process of Al alloys using commercial finite element code ABAQUS [12]. The model took into account the incremental changes in sheet-deformed shape, contact area and large deformation effects. The model predicted the nugget growth and residual stresses, but the quantitative comparison of the predicted residual stress with experiments was not presented. Cha and Na (2003) studied residual stress during the RSW process of AISI 304 stainless steels. The correlations between welding conditions and the residual stress were developed. The results were compared with the measured data by X-ray diffraction. However, the residual stress distribution surrounding the spot weld was not presented [13]. Long and Khanna (2003) developed a thermal-electro-mechanical model to predict the residual stress distribution in a spot welded steel joint [14]. They found that the tensile residual stresses have the maximum magnitude at the center of the nugget and the residual stress decreases towards the edge of the nugget. Hou et al. (2007) developed a thermo-elastic-plastic finite element model using commercial software ANSYS [15]. The model predicted the contact pressure at both the faying surface and the electrode-sheet interface. The stress and strain distributions were also determined. Unfortunately, no experimental data was available for validation. Nodeh et al. (2008) employed a finite element program, ANSYS, and developed an electro-thermo-mechanical model to predict electrical potential, temperature and residual stress distributions during spot welding [1]. The results were compared with experimental data achieving from X-ray diffraction. They found that the maximum tensile residual stresses are located at the weld center and reduced toward the outer sides.

There are various ways to measure residual stress, including semi-destructive method (e.g., hole drilling [16]) or non-destructive method (e.g. X-ray diffraction [13] or neutron diffraction [17-20]). X-ray diffraction has been used in the measurement of residual stresses in spot welds. This method only provides the average residual stress distribution in the surface layers of the weld. Neutron diffraction mapping has the ability to obtain residual stress distribution around the weld nugget within the interior of spot welds.

In summary, due to its inherent complexity and the small nugget size (for example, the nugget size is about 5.0 mm in the current study), it is difficult to obtain the adequate and accurate information of the RSW process. In particular, the distribution of residual stress around the spot weld has not been well studied with numerical modeling, and compared with experimental data.

In this study, an electro-thermal and mechanical finite element model is presented to predict

the temperature distribution, nugget size, and residual stress distribution after resistance spot welding. The effects of welding parameters such as applied current, pressure, and weld cycles on residual stress distribution are discussed. The nugget size is compared with optical microscopy and the predicted residual stresses are compared with measurements obtained by neutron diffraction mapping.

Finite Element Modeling

A two-dimensional finite element model was developed to simulate the spot welding process using the commercial code SYSWELD. The model was used to predict the temperature distribution, molten zone, volume fraction of each phase, and residual stress for two sheets spot welding. The electrical-thermal, thermal-metallurgical, and thermo-metallurgical-mechanical analyses were considered in this model.

Electrical-Thermal Model

In the resistance spot welding, the heat is generated within the material being joined by the resistance to the passage of a high current through the metal parts, which are held under a pre-set pressure. Considering the Joule effect as an internal heat source, the electrical-thermal governing equation is presented as

$$\rho \frac{\partial H}{\partial t} - \text{div } \lambda \cdot \mathbf{grad} T - \mathbf{grad} V \cdot \sigma \cdot \mathbf{grad} V - Q = \quad (1)$$

The electrical phenomena in the computational domain are assumed to be governed by the electrokinetic model for a frequency close to 50 Hz:

$$\text{div}(\sigma \cdot \mathbf{grad} V) = 0 \quad (2)$$

where T , V are the temperature and the scalar electrical potential, respectively. ρ , λ , H , and σ represent the density, the thermal conductivity, the enthalpy, and the electrical conductivity of the medium. The full coupling between electrical and thermal phenomena can be governed by the term $\mathbf{grad} V \cdot \sigma \cdot \mathbf{grad} V$ in the heat equation.

Thermal-Metallurgical Model

In this model, the metallurgical transformations are temperature-dependent, and accompanied by latent heat effects which modify temperature distribution. The thermal properties depend on the temperature and material phase. Based on the thermal history at each point in the resistance spot welding process, the phase transformations that may occur in the material are predicted using the semi-empirical models presented below. Different metallurgical phases, which are austenite, ferrite, bainite, and martensite, are taken into account for this study. For the martensitic transformation, the Koistinen-Marburger law is used [21]:

$$p_m(T) = \bar{p}_m (1 - \exp(-b(M_s - T))) \quad \text{for} \quad T \leq M_s \quad (3)$$

where \bar{p}_m represents the volume fraction of martensite obtained at an infinite low temperature (\bar{p}_m is frequently assimilated to 1). M_s is the martensite start temperature, and b is the evolution coefficient of the transformation process, taken as 0.015 in this model [22].

For the phase transformations involving diffusion in steels (austenitic, ferritic, and bainitic transformations), under isothermal conditions, the Johnson-Mehl-Avrami law is used [23]:

$$p(T, t) = \bar{p}(T) \left(1 - \exp \left(- \left(\frac{t}{\tau_R(T)} \right)^{n(T)} \right) \right) \quad (4)$$

where \bar{p} represents the phase proportion obtained after an infinite time at temperature T , τ_R is the delay time, and n is the exponent associated with the reaction rate. The parameters of the

Johnson-Mehl-Avrami model were extracted from the continuous cooling transformation (CCT) diagram according to the cooling rate and were inserted in the FE code in a tabular form.

Thermometallurgical-Mechanical Model

Several types of interactions between thermal and mechanical analyses are considered including the thermal strains, the volume changes due to the transformations, the influence of the phases on the behavior law, and the plasticity induced by metallurgical transformations. In this study, flat-tip electrodes are used, and the mechanical analysis can be uncoupled from the thermometallurgical analysis. The mechanical contact area is equal to the electrothermal contact area, which is assumed to be constant. The total strain rate is partitioned as follows:

$$\dot{\epsilon} = \dot{\epsilon}_e + \dot{\epsilon}_p + \dot{\epsilon}_{tp} + \dot{\epsilon}_{th} \quad (5)$$

where $\dot{\epsilon}_e$, $\dot{\epsilon}_p$, $\dot{\epsilon}_{tp}$, and $\dot{\epsilon}_{th}$ and are elastic strain rate, plastic strain rate, transformation plasticity, and thermal and metallurgical strain rate, respectively.

Residual stress measurement by neutron diffraction

The neutron diffraction method for strain measurement at a reactor source uses a monochromatic beam of neutrons of known wavelength from a monochromator crystal. The atomic planes of certain crystallographic orientation $\{hkl\}$ diffract the neutrons at a scattering angle of 2θ . Then, using Bragg's law of diffraction:

$$\lambda = 2d_{hkl} \sin \theta \quad (6)$$

where λ is wavelength, d_{hkl} is lattice spacing, and θ is diffraction angle.

The spacing between the lattice planes, d_{hkl} , was found by measurement of 2θ . The diffracting lattice planes, $\{hkl\}$, were those with the plane normal parallel to the scattering vector, \vec{Q} , that is defined as:

$$\vec{Q} = \vec{q}_{\text{incident}} - \vec{q}_{\text{diffracted}} \quad (7)$$

where $\vec{q}_{\text{incident}}$ and $\vec{q}_{\text{diffracted}}$ are the neutron beam vectors in the direction of the incoming and diffracted neutrons [24].

For these measurements, a silicon monochromator with $\{211\}$ planes was used, diffracting neutrons with wavelength $\lambda=1.73\text{\AA}$ that gave a scattering angle of $2\theta=95.1^\circ$ from the sample. To identify the diffracting $\{hkl\}$, x-ray diffraction was performed on one of the sample plates and used to generate a plot of intensity vs. 2θ . The plot showed the $\{211\}$ planes to be diffracting for a 2θ of 95.1° .

Experimental procedure

Using the method of neutron diffraction, strain measurements were taken at the High Flux Isotope Reactor (HFIR) Neutron Residual Stress Mapping Facility (NRSF2) at Oak Ridge National Laboratory (ORNL) for 11 spot weld samples of carbon steel AISI 1018. The dimensions of the plates were 30 mm wide and 100 mm long, with a width of 1.6 mm, as shown in [Figure 1](#). The plates were made by varying three process parameters: weld current, weld pressure, and weld

cycle, according to Table 1. The goal of the neutron measurements was to determine how the magnitude and distribution of residual stresses in the plates were affected by varying these input parameters.

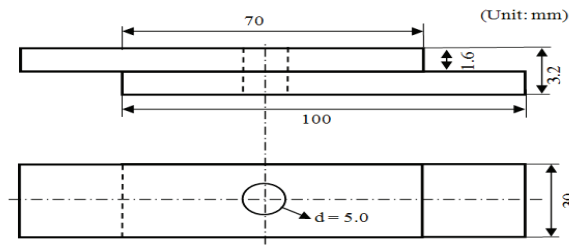


Figure 1. Overall dimensions of weld-boned joint used in the work.

Table 1. Spot weld sample process parameters for residual stress measurements

No	Current (kA)	Force (kgf)	Weld Cycle
1	10	150	18
2	9.5	150	18
3	9.5	150	12
4	9.5	150	24
5	9.5	300	18
6	9.0	150	18
7	9.5	150	15
8	9.5	150	21
9	9.5	200	18
10	9.5	250	18
11	8.5	150	18

Overall dimensions of weld-boned joint used in the work. 1.6 mm thickness steel sheets (Width: 30 mm)

Data was taken at pre-specified locations within each sample. A total of 33 locations symmetrically arranged along the centerlines of top plate, bottom plate, and the interface of two plates were selected, as shown in Figure 2. The boxes in Figure 2 represent gauge volumes within the sample over which all the measured d_{hkl} values are averaged. The dimensions of the gauge volumes correspond to the cross-section of the incident and diffracted neutron beams. The cross-section size was determined by the collimators through which the incident and diffracted neutrons pass, specifically, the areas of the rectangular collimator slits. The sizes of the gauge volumes were necessarily quite small due to the geometry of the nugget size. The incident slits are 1 mm wide and 2 mm tall with offset at 45 mm; the diffracted slits are 1 mm wide in 50 mm snout with offset at 50 mm. The counting times were between 4 and 6 minutes per location. Due to the specimen symmetry, measurements were made along two directions, the longitudinal direction (LD) parallel to the plate, and the normal direction (ND) perpendicular to the plate. The experimental setup for the residual stress measurement in the normal direction is shown in Figure 3.

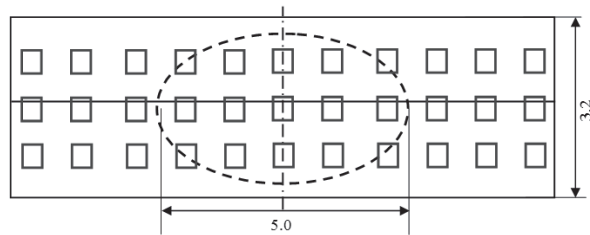


Figure 2 - Data sampling points in the weld plate for neutron diffraction measurement.



Figure 3. Experimental setup for neutron diffraction stress measurement in the normal direction perpendicular to the plate.

The gauge volume was carefully embedded fully within the spot weld samples by using neutron intensity measurements to accurately define the sample surface. The NRSF2 instrument uses seven detectors to collect the diffracted peak profile. These seven detectors are evenly spaced from approximately -15° to $+15^\circ$ out of the horizontal plane of diffraction. From data collected in these seven detectors it was clear that the number of grains contributing to diffraction was low and the Debye ring was “spotty.” To reduce this effect, an omega oscillation of the sample was employed to improve the grain statistics and to reduce the random errors in d-spacing measurements due to the “spotty” Debye ring. This oscillation was shown to improve, but not eliminate entirely, the random errors in d_{hkl} measurement. Data from the seven detectors were corrected using corrections for detector intensity response, and for detector out of plane angle and offset and then summed together before fitting a diffraction profile and determining the 2θ intensity, and full width at half maximum.

Stress-free reference sample

The stress-free lattice spacing was obtained by measuring sliced samples with several comb teeth, as shown in Figure 4. The samples were cut by Electrical Discharge Machining (EDM). Seven sliced samples were cut from the center of the spot weld with the width of 1.5 mm. Different stress-free reference samples were used for the spot weld and the base material. The slice sample was carefully measured using a gauge volume of $1 \times 1 \times 2 \text{ mm}^3$, and the lattice parameter obtained was used to calculate the strain at different points in the plate.

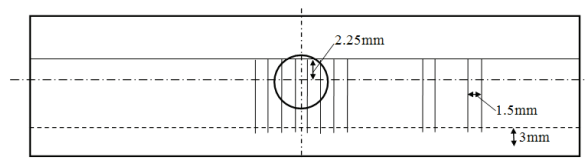


Figure 4. Stress-free d0 spacing sample measurement

Stress and strain calculation

From the measured lattice spacing of the welded sample and stress-free reference samples the elastic strain was calculated according to the following formula:

$$\varepsilon_i = \frac{d_i - d_o}{d_o} \quad (8)$$

where the indices i, j , and k correspond to x, y , and z .

Here d_i and d_o are the lattice spacing, d_{hkl} , for the sample and the reference coupon, respectively, in the three orthogonal directions of the part coordinate system for crystallites with orientation $\{hkl\}$. Also, ε_i represents the corresponding strain in these directions. Since the directions of the measured d_{hkl} ($\vec{d}_x, \vec{d}_y, \vec{d}_z$) coincided with the coordinate axes of the thin-walled plates, the shear contributions to the strain tensor were negated and the calculated strain values ε_i were taken as the principal strains [25].

After calculating the strain with Equation (3), the three orthogonal stress components were found using Hooke's law:

$$\sigma_i = \frac{E_{hkl}}{1 + \nu_{hkl}} \varepsilon_i + \frac{E_{hkl} \nu_{hkl}}{1 + \nu_{hkl}} (\varepsilon_j + \varepsilon_k) \quad (9)$$

where the indices i, j , and k correspond to x, y , and z .

The diffraction elastic constants E_{hkl} and ν_{hkl} in Equation (4) are analogous to the bulk average Young's modulus and Poisson's ratio, respectively, but are specific to planes of a specific $\{hkl\}$ orientation. Due to the presence of numerous crystal orientations within a polycrystalline material, Kröner [26] developed a model for predicting the elastic response in polycrystals composed of randomly oriented crystallites. Behnken and Hauk [27] used the Kröner model to develop an algorithm for calculating polycrystal, hkl -specific elastic moduli using the known values of the single crystal compliance tensor of a material. This algorithm was used here to determine E_{hkl} and ν_{hkl} in the $\{211\}$ direction for a polycrystal from the single crystal elastic constants of alpha iron obtained from Dever [28]. The use of elastic constants intended for cases of random grain orientation is supported by the neutron data, as no significant variation in intensity was observed that would be indicative of significant textures, despite the $\pm 4^\circ$ omega oscillation. The calculated polycrystalline elastic constants in the $\{211\}$ direction for a polycrystal are $E_{hkl} = 205$ GPa and $\nu_{hkl} = 0.29$ for AISI 1018.

Results and Discussions

The samples were cut, polished, and etched to observe the microstructure with optical microscopy. Figure 5(a) shows overall macrostructure of the AISI 1018 spot weld. It shows distinct regions: fusion zone (FZ), heat affected zone (HAZ), and base material. Note that the width of the FZ along the interface of two sheets was ~ 4.4 mm. Figure 5(b)-(d) clearly shows the significant increases of the grain size in the fusion zone compared to the base material.

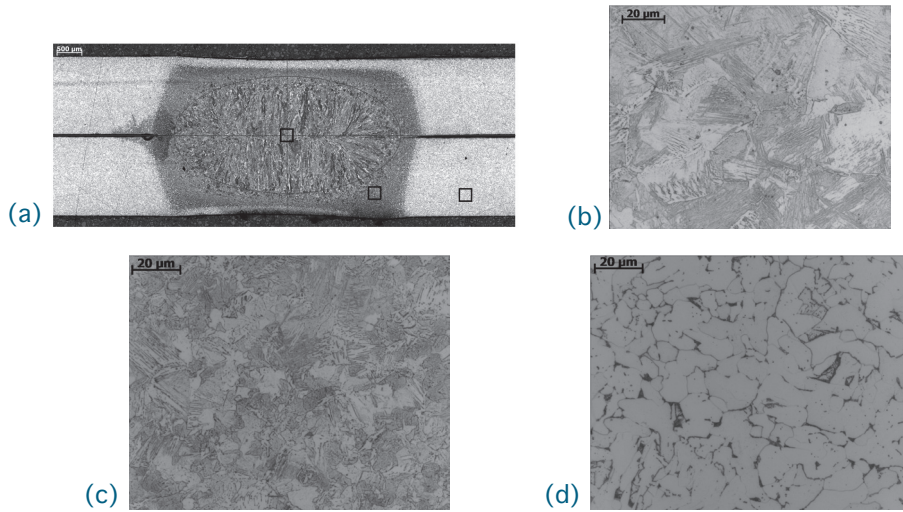


Figure 5. Optical micrographs of AISI 1018 spot weld: (a) overall cross-sectional macrostructure; (b) ~ (d) microstructure of the FZ, HAZ, and base material.

Figure 6 shows the optical macroscopic, microhardness, and residual stress distributions for spot weld sample 1. The maximum hardness is located in the center of the fusion zone (approximately 320 HV), as shown in Figure 6(b). The longitudinal and normal stresses along the center of weld are shown in Figure 6(c) and 6(d). It is noted that the stress distribution is asymmetric for both plates. The reason is probably due to the asymmetrical characters of the spot weld. In the spot welding machine, the bottom electrode sits at an angle. The electrode is filled to have a surface that is parallel with the top electrode but it is not perfect (Figure 7), which results in the asymmetrical characters of the spot weld. The stresses in the longitudinal direction varies in the range of 200 ~ 480 MPa. The stresses in the normal direction varies in the range of -50 ~ 180 MPa. In the following discussion, only the residual stress results at the center of the upper plate are presented.

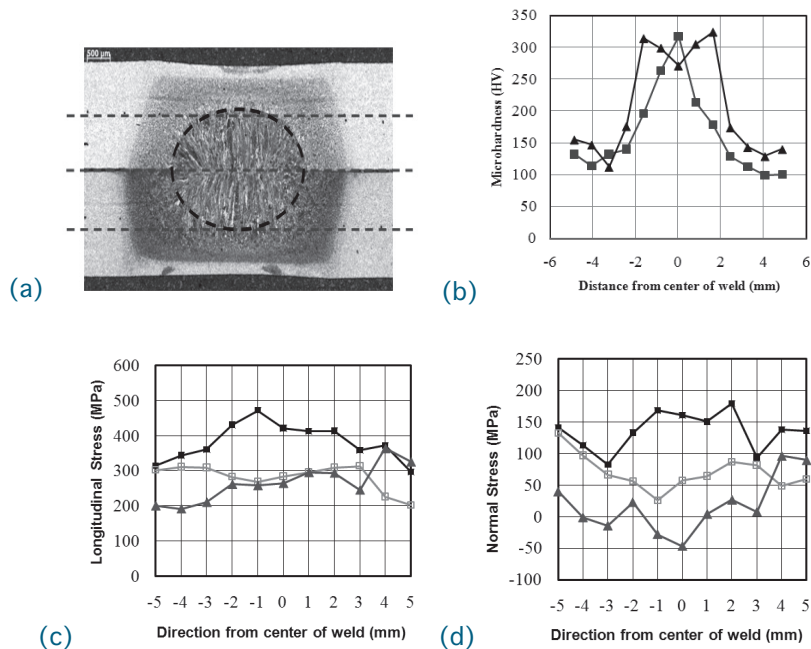


Figure 6 – (a) optical macroscopic of spot weld sample 1; (b) microhardness along the center of top sheet ($Y=0.8$) and bottom sheet ($Y=-0.8$); (c) longitudinal stress; (d) normal stress along the center of top sheet ($Y=0.8$), bottom sheet ($Y=-0.8$), and the interface of two sheets ($Y=0$).

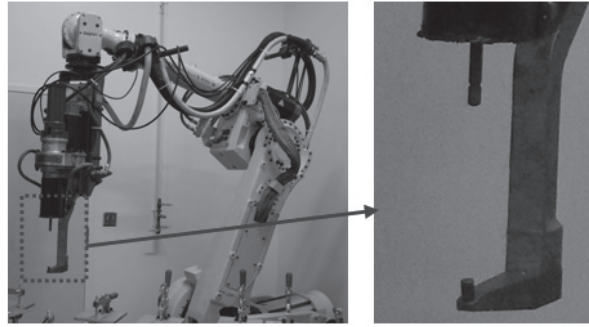


Figure 7. Resistance spot welding system in CAVS extension, the bottom electrode surface is not perfectly parallel to the top electrode surface.

The strain and stress measurements were carried out both in the longitudinal direction parallel to the weld sample and the normal direction perpendicular to the weld sample. Various welding process parameters are studied including weld current, weld pressure, and weld cycle for 11 samples. Figures 8-10 show how residual stress in the LD and ND direction changes as a function of position of the samples for different process parameters. In general, the residual stress at the fusion zone is higher than that at the base materials. The maximum residual stresses are between 400 ~ 570 MPa for longitudinal stress and 160 ~ 230 MPa for normal stress. The maximum residual stress slightly depends on the weld cycles and weld currents; although the increase of weld cycles or weld currents may increase the nugget size. Figure 9 clearly shows the residual stresses decrease with increasing weld pressures, which is consistent with the results in Ref. [13].

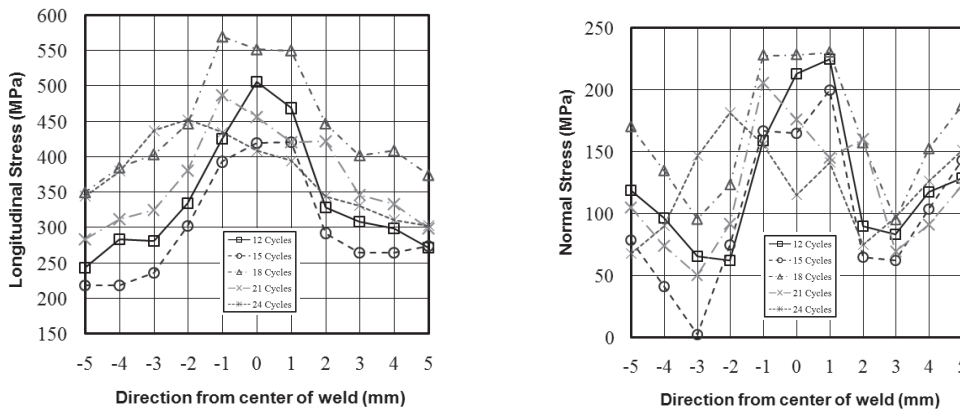


Figure 8. Residual stress variation along (a) longitudinal direction, (b) normal direction of the weld sample for different weld cycles.

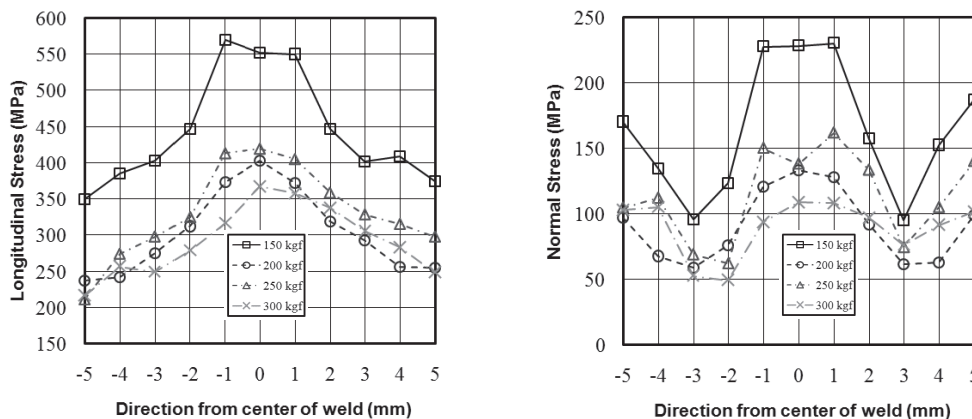


Figure 9. Residual stress variation along (a) longitudinal direction, (b) normal direction of the weld sample for different weld pressures.

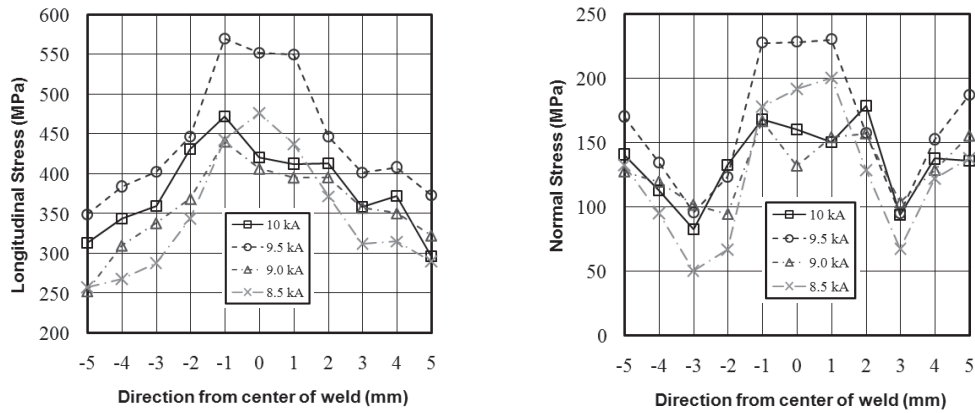


Figure 10. Residual stress variation along (a) longitudinal direction, (b) normal direction of the weld sample for different weld currents.

The comparison between calculation and experiments shows good agreement at the end of heating. Figure 11 compares the sizes of molten zone and heat affected zone obtained numerically and experimentally for sample No. 4. The nominal weld current is 9.5 kA for the experiment and the effective weld current is 8.0 kA used in the simulation. The difference of weld currents can be attributed to the power efficiency, and thermal and electrical contact resistance difference. Figure 12 shows the predicted longitudinal residual stress distribution with SYSWELD. The results were compared with experimental results shown as data in Figure 12.

As mentioned earlier, the asymmetrical characters of the spot weld due to the electrode geometry (Figure 7) may cause the asymmetrical residual stress results. Therefore, it is difficult to quantitatively compare the modeling and experimental results. However, the results show qualitatively agreements between experimental and numerical data. The most significant residual stresses are places at the edges of the fusion zone, where the phases are the mixture of the ferrite and martensitic phases.

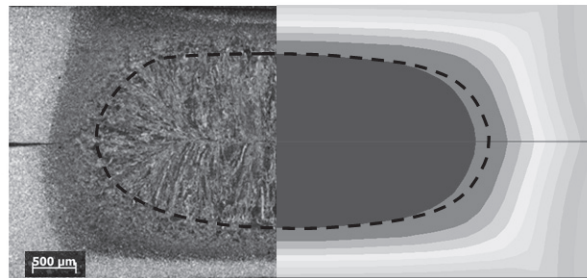


Figure 11. Comparison between numerical and experimental nugget size at the end of heating for sample No. 4.

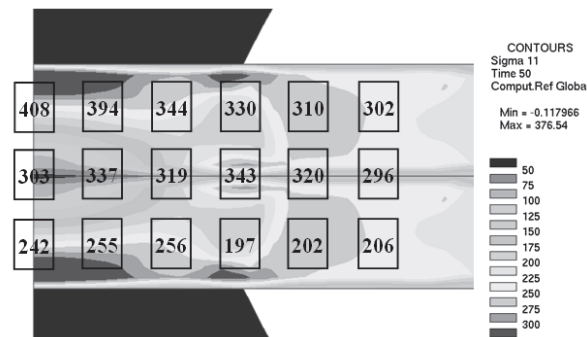


Figure 12. Predicted longitudinal residual stress distribution in the spot weld and compare with experimental results (shown as data in the figure) for sample No. 4.

Conclusions

1. Microstructure, nugget size, and hardness were examined for AISI 1018 spot weld samples. The grain size greatly increased in the fusion zone, compared with the base material. The hardness in the fusion zone is about 320 HV, which is higher than that in the base material.
2. Residual stresses were measured using neutron diffraction under different process parameters. The results show that the maximum residual stress slightly depends on the weld cycles and weld currents, although the increase of weld cycles or weld currents may increase the nugget size. The residual stresses decrease with increasing weld pressures.
3. A thermal-electrical and mechanical finite element model was developed to simulate the spot welding process and complement the experimental data. The simulation results compare well with the measured nugget size and stress distribution.

References

1. Nodeh, I.R., Serajzadeh, S., Kokabi, A.H., "Simulation of Welding Residual Stresses in Resistance Spot Welding, FE Modeling and X-ray Verification," *Journal of Materials Processing Technology*, 205 (2008) 60-69.
2. Paradowska, A., Price J.W.H., Ibrahim, R., and Finlayson, T., "A Neutron Diffraction Study of Residual Stress due to Welding," *Journal of Materials Processing Technology*, 164-165 (2005) 1099-1105.
3. Nied, A.H., "The Finite Element Modeling of the Resistance Spot Welding Process," *Welding Journal*, Vol. 63, No. 4, 1984, pp. 123s-132s.
4. Han, Z., Orozco, J., Indacochea, J. E., and Chen, C.H., "Resistance Spot Welding: A Heat Transfer Study," *Welding Journal*, Vol. 68, No. 9, 1989, pp. 363s-371s.
5. Gould, J. E., "An Examination of Nugget Development During Spot Welding, Using Both Experimental and Analytical Techniques," *Welding Journal*, Vol. 66, No. 1, 1987, pp. 1s-10s.
6. Tsai, C.L., Jammal, O.A., Papritan, J.C., and Dickinson, D.W., "Modeling of Resistance Spot Weld Nugget Growth," *Welding Journal*, Vol. 71, No. 2, 1992, pp. 47s-54s.
7. Cho, H.S., and Cho, Y.J., "A Study of Thermal Behavior in Resistance Spot Welds," *Welding Journal*, Vol. 68, No. 6, 1989, pp. 236s-244s.
8. Wei, P.S., and Ho, C.Y., "Axisymmetric Nugget Growth During Resistance Spot Welding," *ASME Journal of Heat Transfer*, Vol. 112, No. 2, 1990, pp. 309-316.
9. Schroeder, R., and Macherauch, E., "Calculating Thermal and Residual Stresses in Resistance Spot Welded Joints Using Different Thermo-Mechanical Characteristics for the Material," *Schweissen und Schneiden*, Vol. 35, 1983, pp. 270-276.
10. Anastassiou, M., Babbit, M., Lebrun, J.L., "Residual stress and microstructure distribution in spot welded steel sheets: relation with fatigue behavior," *Mater. Sci. Eng. A* Vol. 123, 1990, pp. 141-156.
11. Khan, J.A., Xu, L., Chao, Y.J., and Broach, K., "Numerical Simulation of Resistance Spot Welding Process," *Numer. Heat Transfer, Part A*, 37, 2000, pp. 425-446.
12. Sun, X., Dong, P., "Analysis of aluminum resistance spot welding processes using coupled finite element procedures," *Weld J.*, 2000, 79(8): 215-s-21-s.
13. Cha, B.W., and Na, S.J., "A Study on the Relationship Between Welding Conditions and Residual Stress of Resistance Spot Welded 304-Type Stainless Steels," *Journal of Manufacturing Systems*, Vol. 22, No. 3, 2003, pp. 181-189.

14. Long, X., and Khanna, S.K., "Numerical Simulation of Residual Stresses in a Spot Welded Joint," *Journal of Engineering Materials and Technology*, Vol. 125, 2003, pp. 222-226.
15. Hou, Z., Kim, I., Wang, Y., Li, C., and Chen, C., "Finite Element Analysis for the Mechanical Features of Resistance Spot Welding Process," *Journal of Materials Processing Technology*, 185 (2007) 160-165.
16. Pang, J.W.L., Preuss, M., Withers, P.J., Baxter, G.J., Small, C., "Effects of Tooling on the Residual Stress Distribution in an Inertia weld," *Mater. Sci. Eng. A* 356 (1-2) (2003) 405-413.
17. Paradowska, A., Price, J.W.H., Ibrahim, R., Finlayson, T., "A neutron diffraction study of residual stress due to welding," *Journal of Materials Processing Technology*, Vol. 164-165, 2005, pp. 1099-1105.
18. Paradowska, J.W.H. Price, R. Ibrahim, T.R. Finlayson, R. Blevins, M. Ripley, "Residual stress measurements by neutron diffraction in multi-bead welding," *Physica B: Condensed Matter*, Vol. 385-386, 2006, pp. 890-893.
19. S. Pratihari, M. Turski, L. Edwards, P.J. Bouchard, "Neutron diffraction residual stress measurements in a 316L stainless steel bead-on-plate weld specimen," *International Journal of Pressure Vessels and Piping*, Vol. 86, 2009, pp. 13-19.
20. C. Ohms, R.C. Wimpory, D.E. Katsareas, A.G. Youtsos, "NET TG1: Residual stress assessment by neutron diffraction and finite element modeling on a single bead weld on a steel plate," *International Journal of Pressure Vessels and Piping*, Vol. 86, 2009, pp. 63-72.
21. Koistinen, D.P., and Marburger, R.E., A General Equation Prescribing the Extent of Austenite-Martensite Transformation in Pure Fe-C Alloys and Plain Carbon Steels, *Acta Metall.*, 7 (1959) 417-426.
22. ASM Handbook, Welding, Brazing, and Soldering, Vol. 6, ASM International, Material Park, OH (2005) 438.
23. SYSWELD 2005 Reference Manual, ESI Group (2005)
24. Allen, A.J., Hutchings, M. T., Windsor, C. G., "Neutron Diffraction Methods for the Study of Residual Stress Fields," *Adv. Phys.*, 34 (1985) 446-447.
25. Winholtz, R. A., 2003, "Characterization of macrostresses," in *Analysis of Residual Stress by Diffraction using Neutron and Synchrotron Radiation* (Ed. M.E. Fitzpatrick, A. Lodini), pp. 60-77 (Taylor and Francis, London and New York)
26. Kröner, E., 1958, "Berechnung der Elastischen des Vielkristalls aus den Konstanten des Einkristalls," *Z. Physik* 5, pp.504-518
27. Behnken, H., Hauk, V., 1985, "Berechnung der röntgenographischen Elastizitätskonstanten des Vielkristalls aus den Einkristalldaten für beliebige Kristallsymmetrie," *Z. Metallkde*, Vol. 77, pp.620-625
28. Dever, D. J., 1972, "Temperature Dependence of the Elastic Constants of α -Iron Single Crystals: Relationship to Spin Order and Diffusion Anomalies," *J. Appl. Phys.*, Vol. 43, p.3293

Acknowledgements

This work was also supported by the Center for Advanced Vehicular Systems (CAVS) funding.

Presentations/Publications/Patents

1. Wang, L., Felicelli, S.D., Bammann, D., Hubbard, C.R., “Computational and Experimental Analysis of Residual Stresses in Resistance Spot Welding,” International Conference WELDS 2009, Fort Myers, FL, June 24-26, 2009

G. Joining Strategy Steering Committee Project

Principal Investigator: William Charron
Ford Motor Company
Manager – Manufacturing Collaborative Program
USCAR 30200 Mound Road
6000 Mercury Drive
Bldg: FN1 MD: 150 Cube: AL-008
Dearborn, MI 48126
(313)-805-6628; email: wcharron@ford.com

Technology Area Development Manager: William Joost
(202) 287-6020; e-mail: william.joost@ee.doe.gov

Contractor: United State Automotive Materials Partnership (USAMP)
Contract No.: DE-FC05-02OR22910 through the National Energy Technology Laboratory

Objective

- Identify gaps in technology pertaining to the joining of advanced high-strength steels (AHSS) in automotive applications.
- Develop a roadmap of projects to achieve solutions to the gaps identified in joining technology.
- Facilitate the undertaking of these projects.

Approach

- Retain the services of a recognized expert or experts within the industry to conduct a thorough investigation of joining technologies applicable to AHSS in automotive applications and to identify areas where improvements in joining capabilities are needed.
- Using the results and recommendations of the investigation, develop a roadmap for the resolution of technological gaps identified by the investigation.
- Using the roadmap as a guide, promote the undertaking of projects to develop new joining technologies suitable for use in joining AHSS in automotive applications.

Milestone, metrics and Accomplishments

During the period October 1, 2008 to September 30, 2009 the following items have been accomplished.

- A Request for Quote was issued and a qualified vendor was selected.
- The vendor initiated and completed the investigation of current technologies and potential new processes. Gaps between current joining technologies and future needs were identified.
 1. Letters of introduction were prepared and delivered
 2. Formatted interview forms were prepared and administered
 3. Interviews were conducted with Original Equipment Manufacturers (OEM) representatives and North American steel company representatives

4. European steel suppliers were interviewed
 5. Data collected in the interview process was collated
 6. Detailed literature searches and patent searches were conducted
 7. Interaction with the National Laboratories has been completed
 8. A final report was submitted to the Joining Strategy Steering Committee (JSSC)
- Various roadmaps from other projects were reviewed by the JSSC. The desired format was selected.
 - The JSSC is presently evaluating a draft of the final report submitted by the vendor.

Future Direction

During the period October 01, 2009 to September 30, 2010, the JSSC project plans to:

- Submit final report to A/SP on the gap analysis study.
- Review the results of the JSSC project with:
 - The A/SP Joining Project Team
 - The A/SP Joint Policy Council (JPC)
 - The Joint Policy Board (JPB).
- Begin the preparation of future A/SP projects as identified and prioritized in the Roadmap.
- Expand Roadmap obtain similar data from other industries such as heavy truck, marine, armed service national labs, heavy equipment, etc. The additional data will be embedded into the existing roadmap to create a comprehensive and complete document to satisfy the project goal.

Introduction

Current and future vehicle designs are faced with several stringent requirements that impose conflicting demands on the vehicle designers. Safety must be improved while weight and cost are contained or even reduced. Advanced high-strength steels, judiciously selected and applied, are currently the best candidates offering low-cost (compared with aluminum, magnesium and plastics/composites), reliable materials for meeting these mandates. As structural components are optimized and thinner gauge, advanced high strength steels are employed in greater degrees, new technologies to join the AHSS components are required if the full benefits of the AHSS components are to be achieved.

Discussion

In order to comply with evolving requirements for fuel economy, durability and passenger safety; automobiles must incorporate the increased use of mass-efficient materials. These mass-efficient materials include various grades of AHSS. On-going research by the steel industry continues to produce new classes of AHSS having improved strength, durability and formability

Joining technologies now in use with current steels are well understood and are efficient methods of joining together components formed from commonly used steels. However, to fully achieve the potential for mass reduction and vehicle strength offered by the new grades of AHSS, it is necessary to efficiently join together components made of these evolving AHSS. Current joining technologies, while functional, do not offer optimum joining solutions for use with AHSS components.

It is desirable to rapidly develop new joining technologies for use with AHSS. To accomplish this goal, the Joining Strategy Steering Committee has been formed within the Auto/Steel Partnership (A/SP) and tasked with creating an overall strategy for the development of technologies to efficiently join AHSS automotive components. This overall joining strategy needs to be developed then agreed to and acted upon by the automotive industry. This objective is best achieved by:

- Retaining the services of a recognized expert in industry who can bring credibility and technical expertise to the project.
- Conducting a thorough review of existing joining technologies.
- Conducting a thorough study of promising new joining methodologies from all industries that have the potential for cost-effective application with AHSS in automotive applications.
- Preparation of an organized, orderly sequence of steps and objectives (i.e. a roadmap) to guide the development of these new technologies for automotive applications
- Implementation and execution of specific projects which will develop the technologies identified as needed to fulfill the objectives of the roadmap.
- Transfer the joining technologies thus developed to steel manufacturers and automotive manufacturers for implementation in large scale production processes.

In August 2009, the selected vendor completed the Gap Analysis Report and submitted the report to the Joining Strategy Steering Committee for review. The vendor's gap analysis study was conducted using face-to-face interviews of industry experts, detailed surveys seeking the opinions and knowledge of automotive manufacturing leaders and by travel to centers of technical leadership in Europe and North America. The study participants included; three domestic auto Original Equipment Manufacturers (OEMs), seven steel producers, three universities, two US National Laboratories, two international research institutes and seven commercial technology providers.

The data thus acquired was organized and summarized to highlight technical challenges, infrastructure challenges, desired outcomes and potential solutions to joining technology gaps. Various methods of joining steels and evaluating the acceptability of the joints were evaluated, including:

- Laser Welding and Brazing
- Laser Hybrid Welding
- Adhesive Bonding
- Mechanical Joining
- Friction Stir Welding (FSW)
- Friction Stir Spot Welding (FSSW)
- Resistance Spot Welding (RSW)

- Deformation Resistance Welding (DRW)
- CAE Modeling
- Non-Destructive Evaluation (NDE)

Using the summarized data, the vendor developed a comprehensive set of gaps and identified sixty-five potential projects for possible inclusion in a roadmap of projects to close the identified gaps. The list of sixty-five projects was refined to thirty-four projects recommended for accomplishment. These were further refined to seventeen high priority projects. These included:

- Four for RSW work
- Four for laser welding
- One for laser brazing
- One for arc welding
- Two for adhesive bonding
- Two for mechanical joining
- One for friction stir welding
- One for modeling
- One for NDE

After an initial review of the completed Gap Analysis Report, the JSSC was not fully satisfied with the organization, structure and summary of the report. The vendor was given constructive comments from the JSSC and was asked to revise the final report accordingly. As of September 30, 2009, the vendor is working on the desired revisions. Once the JSSC has accepted the revised report, it will be reviewed with the A/SP Joining Technologies project team then work will begin on creating the roadmap of projects recommended to address technology gaps for joining AHSS.

Conclusions

The JSSC has selected and retained a vendor having the required skills and expertise to facilitate the necessary studies. The vendor has completed the process of summarizing current joining technologies and identifying new joining technologies having the potential for use with AHSS. Once the final report has been accepted, the JSSC will use the information generated to undertake the task of developing a roadmap of projects needed to further explore promising new joining technologies identified by the vendor's study.

¹Denotes project 310 of the Auto/Steel Partnership (A/SP), the automotive-focus arm of the American Iron and Steel Institute (AISI). See www.a-sp.org. The A/SP co-funds projects with the DOE through a Cooperative Agreement between DOE and the United States Automotive Materials Partnership (USAMP), one of the formal consortia of the United States Council for Automotive Research (USCAR), set up by Chrysler Group LLC, Ford Motor Company and General Motors Company to conduct joint, pre-competitive research and development. See www.uscar.org.

H. Development of Steel Fastener Nano-Ceramic Coatings for Corrosion Protection of Magnesium Parts

Principal Investigator: Jinghong Fan
Mechanical Engineering
Alfred University
1 Saxon Drive
Alfred, NY 14802
(607)871-3781; e-mail:fanjing@alfred.edu

Principal Investigator: Xingwu Wang
Electrical Engineering
Alfred University
1 Saxon Drive
Alfred, NY 14802
(607)871-2130/2548; e-mail:fwangx@alfred.edu

Technology Area Development Manager: William Joost
(202) 287-6020; e-mail: william.joost@ee.doe.gov

Manager: Richard Osborne, GM
(586) 575-7039; e-mail: Richard.osborne@gm.com

Contractor: U.S. Automotive Materials Partnership (USAMP)
Contract No.: Automotive Metals Division (AMD704)

Objective

- The objective of this work is to find, develop, and validate the best coatings on steel components and sub-systems to effectively stop the galvanic electric current between steel (cathode) and magnesium (Mg) parts (anode) and to develop cost-effective techniques to solve the galvanic corrosion problems for fasteners of magnesium parts.

Approach

- Thin film coatings of ceramics will be used to electrically and effectively isolate steel bolts, nuts, and washers from Mg parts to stop the galvanic electric current so that the Mg parts can be protected from galvanic corrosion.
- An engineering-science-and-testing-based approach will be used to select the ceramic materials and film thickness for the thin coating layers.
- Comprehensive analyses through various testing of corrosion, characterization of mechanical property and material microstructure, and multiscale simulations at the atomic, nanoscale, and micron scale.
- Transfer knowledge and technology to industry for high volume process.

Accomplishments

- Successfully coated flat steel test specimens with Aluminum oxide and Silicon nitride.
- Demonstrated that nano-ceramic coatings are shown to increase impedance modulus more than 2 orders of magnitude.
- Indicated that coatings are pre and post strain tolerant under 5 wt. % NaCl solution corrosion environment.
- Discovered that nanoparticle size is very important for strength and ductility.
- Learned how to characterize electrochemical results relative to fastener coating barrier corrosion performance.
- Performed corrosion tests that indicated that continuous uniform Si_3N_4 coatings provide a significant barrier.
- Initial cost analyses predicts piece price might be as low as (\$0.005)

Future Direction

- Define coating parameters that produce nano-size particle coating that are continuously uniform.
- Investigate need for multi-layer coatings.
- Produce and provide various levels of coated fasteners for testing by the MFERD (Magnesium Front End Research and Development) corrosion team.
- Refine cost model and potential coating unit price.

Introduction

Several items currently drive the need of this project to developing high fidelity, cost-effective coating techniques for corrosion protection of fasteners. The first item relates to the strong desire of original equipment manufacturers (OEMs) to increase fuel economy and reduce CO₂ emissions thereby requiring increased use of lightweight metals such as magnesium, the lightest structural metal. The second item is that two of the three major technological difficulties in the usage of magnesium alloys are related to corrosion and fasteners. The third is cost savings related to reduced engineering and speed to market for a product. The fourth is the need for improved Mg/steel joint reliability and durability through completing this USAMP project. Currently evaluated mitigation solutions have failed to meet corrosion validation requirements, which lead us to a realization that a comprehensive R & D study, involving fundamental understanding, various material choices, and innovative concepts, is necessary to find the best solutions for corrosion protection when joining Mg components with steel fasteners and to other metal components.

Progress

During this annual period, several nano-ceramic coating process were developed for carbon steel substrates. The main effort was in two parts: nano-ceramics coating on flat 1050 steel coupons and preliminary salt mist spray testing on coated fasteners.

Nano-coating on flat 1050 steel coupons

Surface treatment

We follow the surface treatment procedure discussed in detail in the annual report of 2008. There was no intention to completely remove the scratch lines, as the ultimate objective of the study is to coat the fasteners which may have grooves and trenches. Since the carbon steel is known for its inclusion impurities, an FEI Co. Quanta 200F environmental scanning electron microscope (ESEM) was utilized to characterize such impurities, along with an attached energy dispersive X-ray spectroscopy (EDS) module. There are approximately 220 defects per mm². The sizes of the defects vary. An “inclusion” defect appears to be round, with its “diameter” being approximately 10 micrometers. The composition in defect area besides iron, sulfur, calcium, manganese and other elements are revealed.

Corrosion of bare steel

Impedance characteristics of an uncoated-polished 1050 carbon steel control sample were measured by Electrochemical Impedance Spectroscopy (EIS) measurements, with a wet cell area of 3 cm². The surface area was exposed to the wt 5% NaCl solution. In Figure 1, the impedance modulus is plotted as a function of the frequency for a control sample (the bottom curve). This result indicates that polished 1050 carbon steel itself did not resist corrosion. Visually, corrosion was observed after the 30 minutes soaking with the salt water.

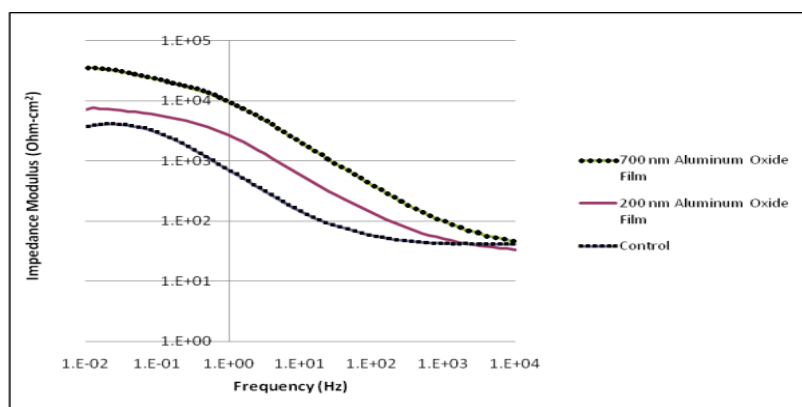


Figure 1. Impedance modulus is plotted as the function of the frequency.

Aluminum Oxide Coatings on 1050 Carbon Steel Substrates

Aluminum oxide thin films were deposited via the electron beam evaporation technique. A film was deposited at a substrate temperature of 190°C, with a deposition rate of 1 Å/s and a film thickness of approximately 200 nm (Film A1). The SEM shows the number of the defects per unit area is reduced from approximately 220 defects per mm² to approximately 20 defects per mm². That is, compared with the substrate before the coating, most defect areas are covered by the aluminum oxide coatings.

Coating thickness effects

In Figure 1, the impedance modulus comparison between coated and uncoated specimens is plotted as a function of the frequency. In comparison with the impedance modulus curve for the uncoated 1050 carbon steel substrate (bottom curve), the impedance modulus of the coated sample is higher than that of the control, at a given frequency. For example, at 0.01 Hz, the impedance modulus of the coated sample with thickness of 200 nm (denoted as coating Film

A1) is approximately 7.1×10^3 ohm-cm² (middle solid line in Figure 2), and of thickness of 700 nm (Film A2) is 3.6×10^4 ohm-cm² (top line) while that of uncoated 1070 steel is 3.7×10^3 ohm-cm² (bottom line). We believe the lowest frequency is important for the corrosion behavior at the service condition, thus in this report we use the corrosion behavior of 0.01 Hz for comparison.

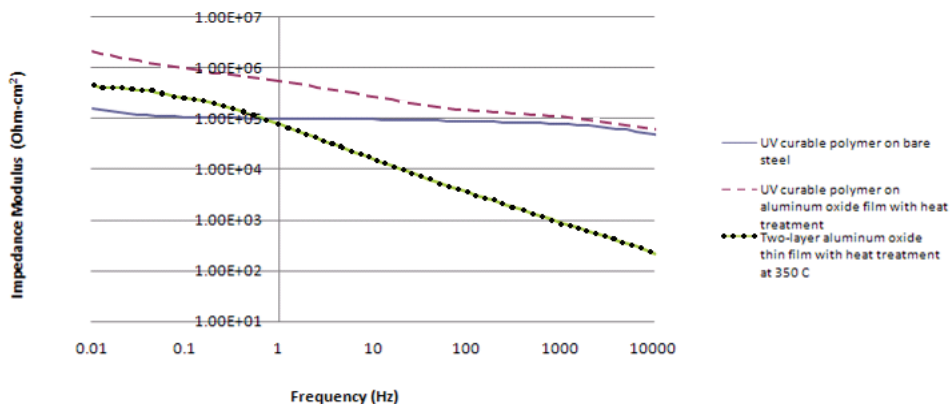
Coating heat treatment effects

In a furnace with the ambient atmosphere, the post deposition heat treatment was conducted for a film fabricated with the same deposition conditions as Film A1, with the film thickness of approximately 150 nm. The heat treatment temperature for this sample (Film A3) was approximately 350°C, and the heat treatment time duration was approximately 40 min. At a given frequency, the impedance modulus of Film A3 is always higher than that of Film A1. Specifically, at 0.01 Hz, the impedance modulus of Film A3 is 2.6×10^4 ohm-cm², which is higher than that of Film A1 (7.1×10^3 ohm-cm²).

Effects of double coating layers

For another film fabricated under the same condition as Film A3, after the heat treatment, an additional layer of aluminum oxide film with the thickness of 120 nm was deposited. The total thickness of the coating after the second deposition is 270 nm (Film A4). In Figure 2, the plot for the impedance modulus for Film A4 with heat treatment is illustrated (green curve). At 0.01 Hz, the impedance modulus value for Film A4 is approximately 4.6×10^5 ohm-cm², which was about 60 times higher than that of a single layer coating (Film A1).

Figure 2. Comparison of coating effects between double layers with heat treatment (line with dot), UV curable



polymer on bare steel (solid line), and UV curable aluminum oxide film with heat treatment (top dashed line).

Effects of coating with UV curable polymer

A layer of UV-curable materials containing cerium oxide material was applied on top of the bare 1050 steel substrate (Film UV). In Figure 2, the curve with dot is the impedance modulus plot for Film UV. At 0.01 Hz, the impedance modulus value for Film UV is approximately 1.6×10^5 ohm-cm². In addition, a layer of the UV curable materials was applied onto a film fabricated under the heat-treatment conditions as Film A4, Film UV-A4. In Figure 2, the top dashed curve is the impedance modulus plot for Film UV-A4. At 0.01 Hz, the impedance modulus value of Film UV-A4 is approximately 2.1×10^6 ohm-cm² which is about 4.5 times higher than A4 and 280 times larger both Film A4 and Film A1 respectively.

Silicon Nitride Coatings on 1050 Carbon Steel Substrates

Coating Processing

Silicon nitride thin films were either coated by the plasma assisted atomic layer deposition (ALD) technique or the plasma enhanced chemical vapor deposition (PECVD) techniques. The substrate temperatures were 250 - 300°C. The precursors for plasma ALD included SiH[N(CH₃)₂]₃, nitrogen gas, and hydrogen gas. The precursors for PECVD included silane (100% or 3% in argon), ammonia, and/or nitrogen gas. There were two groups for the film thickness. The thickness, t, for the first group is 20 - 60 nm, and the thickness for the second group is 300-850 nm.

Layer thickness effects

In Figure 3, the lowest dashed curve at 1 Hz is the impedance modulus plot for 20 nm silicon nitride film, the dashed curve above it at 1 Hz is for 40 nm silicon nitride film, and the solid curve is for 60 nm silicon nitride film. At 0.01 Hz, the impedance modulus value for the 60 nm films is approximately 6.1×10^4 ohm-cm², which is higher than both impedance modulus values for the 40 nm and 20 nm films (2.1 - 2.2×10^4 ohm-cm²). The top three curves with higher resistance are for thickness, t, of 300, 600 and 850 nm, the greater the thickness, the higher the electrochemical impedance modulus. Specifically, the maximum impedance at 0.01 Hz for the three coating thickness layers read:

t=300 nm	2.1×10^5	ohm-cm ²
t= 600 nm	4.1×10^5	ohm-cm ²
t=850 nm	14.0×10^5	ohm-cm ²

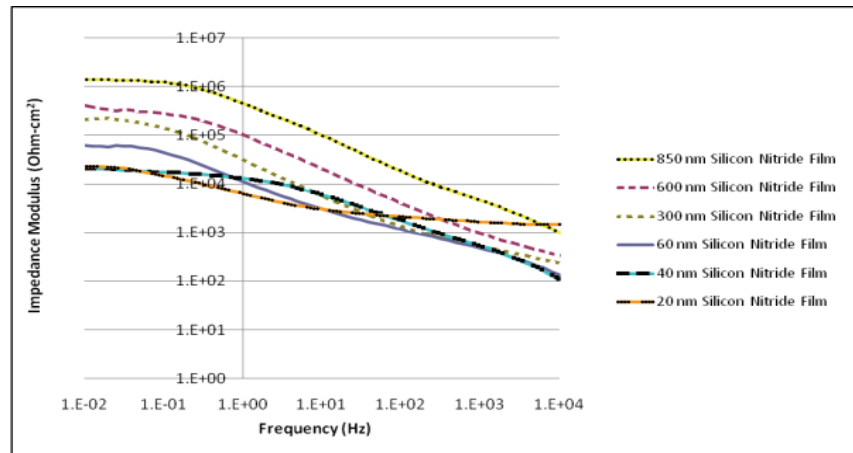


Figure 3. Impedance modulus increases with increasing coated layer thickness.

Mechanism for thickness effects in terms of defects

It has been found that coating layer thickness influences whether the coating completely covers the micro surface defects. Figure 4 shows a perfect surface morphology in a small field for thickness t=600 nm, but for a large region it is found that the thin layer will not adequately cover all the surface defect as shown in the SEM image, Figure 5.

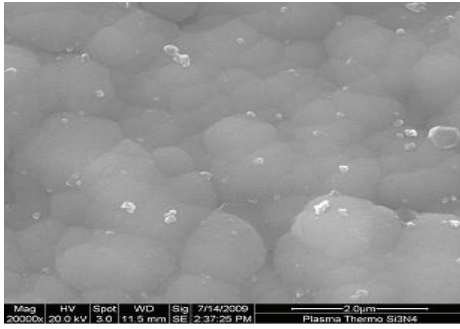


Figure 4. SEM top view with magnification of 20 K, for 600 nm silicon nitride film

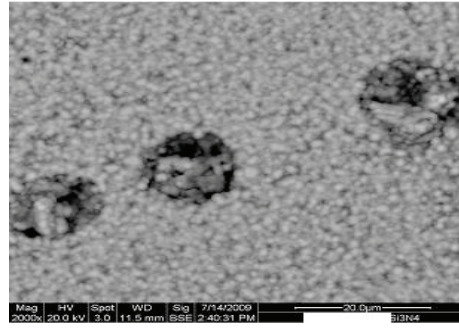


Figure 5. SEM top view with magnification of 2K, for 600 nm silicon nitride film

Conclusion of flat coupon coating

For the aluminum oxide films, the highest impedance modulus value at 0.01 Hz is approximately 4.6×10^5 ohm-cm². With an additional UV curable cerium oxide layer, the impedance modulus value is increased to approximately 2.1×10^6 ohm-cm². For the silicon nitride films, the highest impedance modulus value at 0.01 Hz is 1.4×10^6 ohm-cm² for the film with the thickness of 850 nm. It is estimated that if a UV curable layer was added to the silicon nitride layer, the impedance will be increased about 5 times.

Preliminary salt mist spray testing on coated fasteners

To speed the process for delivery of the nano-coating technology to automotive fasteners applications, corrosion testing has been initiated.

5%NaCl spray corrosion testing for M16 Bolt coated by Silicon Nitride thin film

The salt spray corrosion chamber is shown in Figure 6. The M14 steel specimen used in a GM vehicle was coated by Silicon Nitride through PECVD process with the thickness about 850 nm. The appearance of the steel bolt after 18 days and 21 days, are shown in Figure 7 and 8, respectively. A magnesium plate was fixed to the bolt in Figure 8 creating a steel-Mg galvanic corrosion environment. The weight change of the bolt is given in Table 1. The weight increase after 53 days is 0.069 gram for the steel due to the deposition of the salt particles on the bolt surface.



Figure 6. The salt mist spray corrosion testing chamber.



Figure 7. Overall of the M14 bolt after 18 days.



Figure 8. Overall of the M14 fastener after 21 days

Table 1. Weight change after 53 days in the Environmental chamber

Days	First Day (March 2)	21 days (March 23)	53 days (April 24)
Weight (g)	158.806	158.823	158.895
Weight gain (g)	0	0.017	0.089

GM laboratory corrosion test

Figure 9 shows the feature of M10 steel fasteners after the first cycle of GM corrosion test in the GM laboratory. From the test, following was observed:

1. Fastener pieces coated with 2-D PECVD system has a certain anti-corrosion capability.
2. Non-uniformly coated bolt heads showing red rust.
3. Flat washers indicate no red rust except run-off from bolt heads.
4. GMW3359 (organic Zn-Al coating) showing galvanic corrosion.



Figure 9. Steel fastener/Mg assemble corrosion test conducted at the GM corrosion laboratory after the first testing cycle. The left four are steel fasteners after silicon nitride coating, the right two are GMW3359 (organic Zn-Al coating) which is showing galvanic corrosion.

3 Other series of galvanic corrosion test at AU

Four additional types of galvanic corrosion tests were conducted at Alfred University to find the reason for corrosion of coated fasteners. Testing included both aluminum oxide and silicon nitride coatings. The main results are as follows:

1. Generally speaking, aluminum oxide coated samples have better anti-corrosion performance than the uncoated fasteners. Silicon nitride coated samples are better than the aluminum oxide coated samples.
2. The weak spots of the coated samples are where stains were present. This observation is related to the need for the better substrate preparation before the coating. From Figure 10, it is seen that first corrosion always showed in the area where stains are.
3. Other weak spots are near the edges. For example, four sides of a washer were not completely coated when the coatings were only applied to the stamped side and the un-stamped side of the washer. (This observation indicates the need to tumble the samples during the coating process.)
4. Furthermore, the other weak spots are near the complicated shapes, such as a narrow gap. (This observation is related to the need to uniformly expose all the spots to the chemical vapor.)
5. So far, the silicon nitride coated washer provides better protection than the complex bolt geometry.
6. The six sides of the hexagonal nut are better than the top and bottom faces of the nut. (Presumably, the six sides were better coated than the two faces.)
7. As far as the washer is concerned, the stamped side has much better anti-corrosion performance than un-stamped side.



Figure 10. SiN coated steel washer after 12 days in the environmental chamber. First corrosion always showed in the area where stains are.

Figure 11 shows preliminary VDA (German automotive test procedure) test results for 48 hours of corrosion exposure. The surface of the Mg-plate had general corrosion, the contact area of bolt and plate did not have corrosion via visual observation.

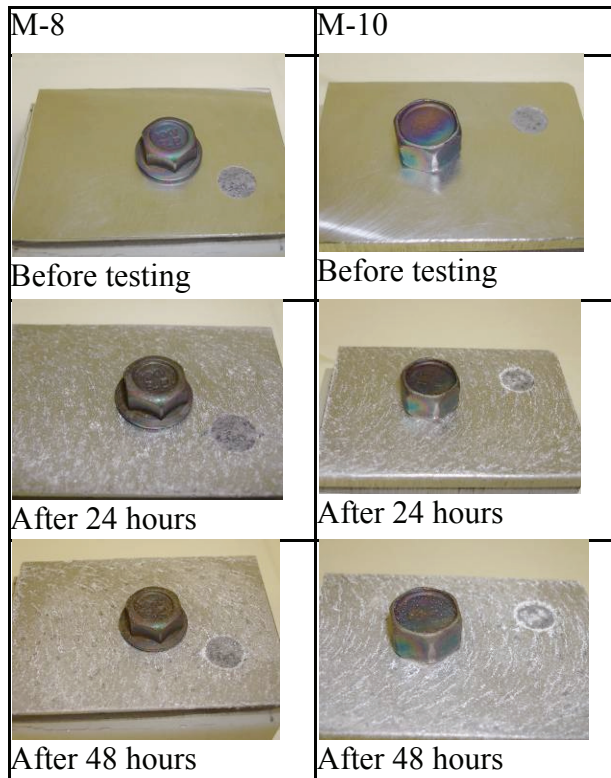


Figure 11. VDA corrosion test M-8 vs. M-10

Conclusions

This research is focused on the barrier layer application of aluminum oxide and silicon nitride thin films on carbon steel substrates. In last year's annual report, we demonstrated the successful verification of the basic concept that nano-ceramic coatings have high corrosion resistance and high strength under the combined mechanical loading and chemical corrosion environment. Therefore, this year's research is more concentrated on the problems related to delivery to industrial applications. The main conclusions are as follows:

1. From the cost model developed in this project, it is seen that the developed technique is cost-effective with the fee coating cost as low as \$0.0015 per 1 micrometer coating thickness. It indicates that this developed technique has great potential for broad application in automotive industry.
2. Two basic nano-ceramic coating technologies are developed. One is aluminum oxide coatings and the other is silicon nitride coatings. Both can reach high impedance modulus.
3. Effect of coating layer thickness is systematically investigated. It is found that under the maximum layer of 850 nm, the thicker the layer and the higher the impedance modulus, the better the coating quality.
4. Mechanisms of the thickness effect are also researched. It is found that the increased coating thickness effects can help bridge defects on the steel surface related to defects. If the coating thickness cannot fully cover the surface defect, then corrosion will occur.
5. Heat-treatment will increase the impedance modulus to improve the coating quality.
6. The combination of UV curable with aluminum oxide coating greatly increases the impedance modulus.